Mar 97

Modeling of ionization phenomena in SiC diodes

Final Technical Report

By

Paolo Lugli
Department of Electronic Engineering,
Università di Roma "Tor Vergata",
00133 Roma (Italy)

United States Army
EUROPEAN RESEARCH OFFICE OF THE U.S. ARMY
London England
CONTRACT NUMBER N68171-96-C-9115
Approved for Public Release; distribution unlimited
R+D no: 8127-EE-01.

6

Chapter 1

Introduction

The theoretical study presented in this report has been triggered by some experimental findings [1] indicating a negative temperature ionization coefficient, that is a breakdown voltage decreasing with temperature. Traditionally, semiconductors disply a positive temperature coefficient, that is the breakdown bias increases with temperature. This is a signature of the intrinsic stability of a device, as under high bias operation, the internal heating of a device immediately translate into an enhancement of the breakdown voltage. On the contrary, a device exhibiting a negative coefficient is intrinsically unstable, as an increase in the internal temperature authomatically favors the device breakdown. For instance, devices with a negative temperature coeffient would distructively react to a sudden current glitch. Furthermore, the presence of hot spots, that is special points of a device where (for instance because of the presence of dislocations) a lot of current is channeled, would also have catastrophic consequences. Figure 1.1 shows a typical 4H-SiC PN structure fabricated by NASA using available commercial substrate.

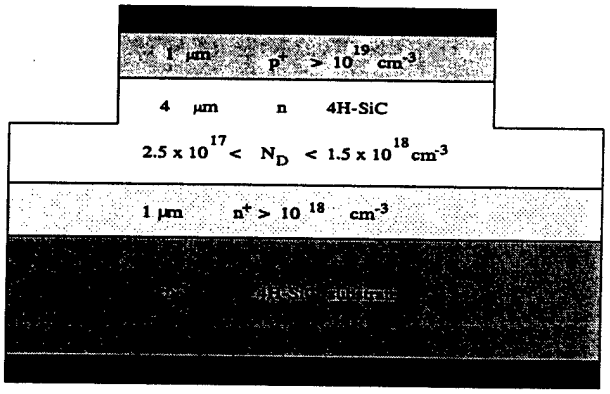

Figure 1.1: *Cross section of the 4H-SiC pn junction diode*

The corresponding IV characteristic is presented in Fig.1.2. In the experimental investigation all diodes showing strong leackage currents or non-vertical breakdown characteristics have been escluded.

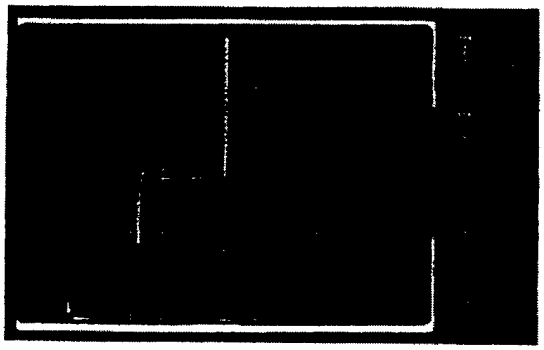

Figure 1.2: *Curve-tracer used for the d.c. IV characteristics*

The experimental technique was based on the measurement of the device response to a sudden voltage pulse with a rise time of about 200 ns. From the temporal evolution of the diode current and voltage, the temperature coefficient has been extracted. An sample of the experimental finding is presented in fig.1.3. For voltage valure below the breakdown voltage, a fast transient response is observed, which is associated to displacement currents in the device.

At higher voltages, a persistent current and voltage is found on the device as long as the voltagestep is present. For 4H-SiC diode (shown in the figure), a positive temperature coefficient is found. On the contrary, all 6H-SiC sample that have been investigated have shown an opposite trend.

The objective of the present work has been to determine wheter intrinsic physical phenomena can be responsible for the anomalous behavior of 6H-SiC diodes. Our study is based on a selfconsistent drift-diffusion approach. The physical basis of the method will be described in Ch. 2, while the numerical implementation is presented in Ch. 3. The method is then applied to a SiC diode and the results discussed in Ch. 4.

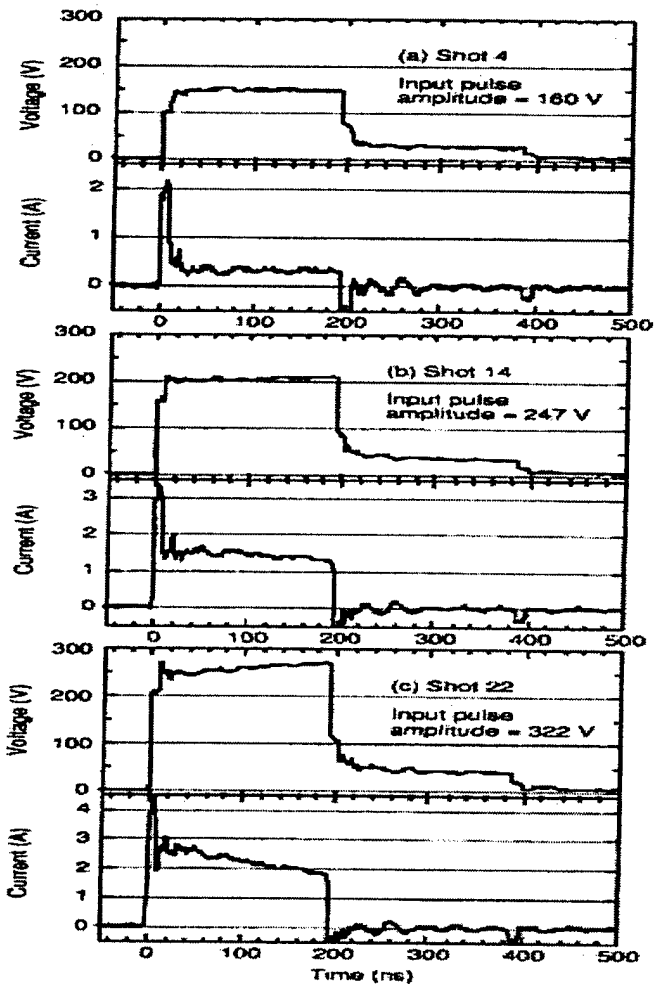

Figure 1.3: *Experimental results on the diode dynamical response*

Chapter 2

Drift-diffusion approach

In this section, we will describe the Drift-diffusion (DD) algorithm, which constitutes the basis of our simulation.

2.1 Drift-Diffusion method

The starting point for any semiclassical transport theory (such as the DD method) is Boltzmann transport equation which describes the evolution of the carrier distribution function in the presence of external perturbations and non homogeneous conditions. The importance of the distribution function is that it contains all microscopic information on the carrier dynamics. In particular, its first three moments are related to the observable of the systems, namely

- carrier concentration

$$n(\mathbf{r},t) = \frac{2}{(2\pi)^3}\int f(\mathbf{r},\mathbf{k},t)d\mathbf{k} \tag{2.1}$$

- mean current density

$$J(\mathbf{r},t) = \frac{2q}{(2\pi)^3}\int \mathbf{v}(\mathbf{k})f(\mathbf{r},\mathbf{k},t)d\mathbf{k} \tag{2.2}$$

- mean energy

$$\langle E(\mathbf{r},t)\rangle = \frac{2q}{(2\pi)^3}\int E(\mathbf{k})f(\mathbf{r},\mathbf{k},t)d\mathbf{k}) \tag{2.3}$$

Directly from Boltzmann equation, it is possible to obtain the differential equations for such observables [2], namely the current continuity equation

$$\frac{\partial n}{\partial t} = \frac{1}{q}\nabla_r J_n \tag{2.4}$$

and the balance equation for momentum and energy,

$$\frac{\partial J_n}{\partial t} = \frac{-2(-q)\nabla_r \mathbf{W}}{m^*} + \frac{q^2 n \mathbf{F}}{m^*} - \left\langle \frac{1}{\tau_m} \right\rangle J_n \tag{2.5}$$

$$\frac{\partial W}{\partial t} = -\nabla_r \mathbf{F}_W + \mathbf{J}_n \mathbf{F} - \left\langle \frac{1}{\tau_E} \right\rangle (W - W^0) + \chi \tag{2.6}$$

where $\mathbf{W}$ is the kinetic energy tensor (W_0 is its equilibrium value), τ_m and τ_E are respectively the average time for momentum-dissipating and energy-dissippating collisions, $\mathbf{F}$ is the electric field.
The equations 2.4, 2.5 and 2.6 are the basis of the so-called "hydrodynamical method" for device simulation (once coupled to Poisson equation). A simpler model can be obtained with some assumptions, as shown below. The starting point is Eq. 2.5 expressed as

$$J_n + \frac{1}{\langle 1/\tau_m \rangle} \frac{\partial J_n}{\partial t} = \frac{-2(-q)\nabla_r \mathbf{W}}{m^* \langle 1/\tau_m \rangle} + \frac{q^2 n \mathbf{F}}{m^* \langle 1/\tau_m \rangle}$$

If we define the mobility as

$$\mu_n = \frac{q}{m^* \langle 1/\tau_m \rangle} \tag{2.7}$$

and assume that the current does not vary considerably in a time $1/\langle 1/\tau_m \rangle$, then we have

$$\mathbf{J}_n = nq\mu_n \mathbf{F} + 2\mu_n \nabla_r \mathbf{W} \tag{2.8}$$

The tensor $\mathbf{W}$ contains two contributions related respectively to thermal and drift motion. In order to simplify Eq. 2.8 the drift component of $\mathbf{W}$ are ignored and the temperature tensor is assumed to be diagonal, so that

$$W_{ij} = \frac{nK_B T_C}{2} \delta_{ij} = \frac{W}{3} \delta_{ij} \tag{2.9}$$

where

$$W = \frac{3}{2} nK_B T_C \tag{2.10}$$

is the kinetic energy density, and T_C the carrier temperature. By inserting Eq. 2.9in Eq. 2.8, we have

$$\mathbf{J}_n = nq\mu_n F + \frac{2}{3} \mu_n \nabla_r W \tag{2.11}$$

By expanding the gradient, and expressing the result in terms of T_C, the current equation becomes

$$\mathbf{J}_n = nq\mu_n \mathbf{F} + qD_n \nabla \mathbf{n} + qS_n \nabla \mathbf{T_C} \tag{2.12}$$

which is indeed called "Drift-diffusion" equation. In 2.12, Two new parameters have been introduced, The diffusion coefficient:

$$D_n = \frac{K_B T_C}{q} \mu_n \tag{2.13}$$

and the Soret coefficient:

$$S_n = n\frac{K_B}{q}\mu_n \tag{2.14}$$

In 2.12 T_C must been known. At low electric fields, the carrier temperature can be taken equal to the lattice one; at higher fields, the energy balance equation has to be solved.

2.2 Generation terms

In Eq. 2.4, an extra term has to be added on the right hand side, which account for generation processes that can alter the carrier concentration. In a device under strong bias, two main processes have to considered, impact ionization and field-assisted ionization via tunneling.

2.2.1 Impact ionization

In the presence of high electric fields, carriers can gain sufficient energy to be able to promote an electron from the valence to the conduction band. Such process, called "impact ionization", produce an additional electron-hole pair in the semiconductor. The multiplication process, when repeated, can lead to the breakdown of the device.

The rate of electron-hole pair production due to impact ionization processes G is given by:

$$G = \alpha_n n v_n + \alpha_p p v_p$$

where α_n is the electron ionization coefficient defined as the number of electron-hole pairs generated per unit length by an electron, v_n is the electron drift velocity and n the electron concentration. The subscript p refers to holes.

The electric field dependence of the ionization coefficients $\alpha_{n,p}$ can be expressed as:

$$\alpha_{n,p} = \alpha_{n,p}^{\infty} exp\left[-\left(\frac{E_{n,p}^{crit}}{E}\right)^{\beta_{n,p}} \right] \tag{2.15}$$

where E is the electric field, E^{crit} is a critical electric field for the ionization process, and $\alpha_{n,p}^{\infty}$ a parameter.

2.2.2 Ionization due to tunneling

Generally, in conventional semiconductors at room temperature, dopants are fully ionized. In special cases, for instance at very low temperature or for dopants creating states deep into the gap, ionization can be only partial. Then the presence of an

electric field can influence the degree of ionization of dopant atoms, via a process called field-assisted tunneling.

The electron generation rate due to field assisted tunneling can be espressed as:

$$G_t = \frac{\partial n_d}{\partial t} = -\frac{n_d}{\tau}.$$

where n_d is the electron concentration on the donor level and τ is the tunneling time.

The temporal evolution of n_d is given simply by:

$$n_d(t) = n_{d0} e^{-\int_0^t \frac{y}{\tau(y)} dy}$$

where n_{d0} is the initial concentration of electrons on the donor atoms. In discrete form:

$$n_{di}^j = n_{doi} e^{-\sum_0^j \frac{j\Delta t}{\tau_i^j}}.$$

The electric field dependence of the tunneling time is given by the equation[4]:

$$\tau^{-1} = \omega \frac{\alpha}{F} e^{(-\frac{\alpha}{F})}$$

where α and ω are given by:

$$\begin{aligned} \alpha &= \frac{4E_d^{\frac{3}{2}}\sqrt{2m^*}}{3eh} \\ \omega &= \frac{12E_d}{\hbar}. \end{aligned} \tag{2.16}$$

E_d being the dopant energy level.

2.3 Mobility

The field dependence of the carrier mobility $\mu(F)$ is given by the relation [5]:

$$\mu_{n,p}(\mathbf{F}) = \left[\frac{1}{1 + \left|\frac{\mu_{n,p}^0 \mathbf{F}}{v_{sat}}\right|^\alpha}\right]^{1/\alpha} \mu_{n,p}^0 \tag{2.17}$$

where α is a constant (typically equal to 1 or 2). The saturation velocity v_{sat} depends on temperature, according to the phenomenological law

$$v_{sat}(\mathbf{T}) = \frac{v_{sat}(0)}{1 + 0.8exp\left(\frac{\mathbf{T}}{600\,K}\right)}. \tag{2.18}$$

In SiC we have $v_{sat}(0) = 4.64 \times 10^7\, cm/s$.

The temperature dependence of the carrier mobility can be expressed as

$$\mu_{n,p}^{0} = \mu_{n,p}^{min} + \frac{\mu_{n,p}^{delta}}{1 + \left(\frac{N_D + N_A}{N_{n,p}^{\mu}}\right)^{\gamma_{n,p}}} \left(\frac{T}{300\,K}\right)^{\alpha_{n,p}} \tag{2.19}$$

where the parameters $\mu_{n,p}^{min}$, $\mu_{n,p}^{delta}$, $N_{n,p}^{\mu}$, $\alpha_{n,p}$ e $\gamma_{n,p}$ depend on the material.

2.4 Thermal effects

Thermal effects due to internal heating can be accounted for via the heat transport equation: [6]

$$\rho c \frac{\partial T_C}{\partial t} - H = \nabla \cdot (k(T_C) \nabla T_C) \tag{2.20}$$

where ρ (kg/m^3) and c $(Joule/kgK)$ are the density and specific heat, respectively, $k(T_C)$ the thermal conductivity and H the local heat, given by the product $\mathbf{J}_n \times \mathbf{F}$. The temperature dependence of ρ and c can be neglected [6]. Furthermore, if we are not interested in the thermal transient behavior, we can set $\partial T_C/\partial t$ to zero, which greatly facilitate the solution of Eq. 2.20 in one dimension.

2.5 Displacement current

For the study of electrical transient, the contribution of the displacement current cannot be neglected. For a 1D structure of length W, the time dependent total current density is

$$J_n = q\mu_n n E + qD_n \nabla n + qS_n \nabla T_C + \frac{\varepsilon_s \varepsilon_0}{W} \frac{dV(t)}{dt}$$

The current can then be written as

$$I(t) = C_0 \frac{dv(t)}{dt} + I_0(t)$$

where $C_0 = \varepsilon \frac{A}{W}$ is called *cold capacitance*, A being the device cross section.
A one dimensional device can therefore be represented as a current generator in parallel to the cold capacitance. At every time step in the simulation, the voltage V must be updated, as it depends on the charge stored in the capacitance.

Chapter 3

Numerical model

In this chapter we will outline the physical approach used in the study and its numerical implementation

3.1 Fundamental equations

As pointed out in the previous section, the fundamental equations of our Drift-Diffusion approach are [6]

- Poisson equation

$$\nabla \cdot (\epsilon \nabla \Phi) = -q(p - n + N_D^+ - N_A^-) \tag{3.1}$$

- continuity equation for electrons and holes

$$\begin{aligned} \nabla \cdot J_n - q\frac{\partial n}{\partial t} &= qR \\ \nabla \cdot J_p + q\frac{\partial p}{\partial t} &= -qR \end{aligned} \tag{3.2}$$

- current equation for electrons and holes

$$\begin{aligned} J_n &= nq\mu_n F + qD_n \nabla n + qS_n \nabla T_C \\ J_p &= pq\mu_p F - qD_p \nabla p - qS_p \nabla T_C \end{aligned} \tag{3.3}$$

- heat transport equation

$$\rho c \frac{\partial T_C}{\partial t} - J \times F = \nabla \cdot (k(T_C)\nabla T_C) \tag{3.4}$$

The models for R, the generation-recombination rate, for μ_n,μ_p (electron and hole mobility) and for $K(T)$ will be discussed below.

3.2 Discretization

Here we will discuss the various discretization techniques followed.

3.2.1 Continuity equation

By substituting Eqs. 3.3 in 3.2, the following relations are found

$$\frac{\partial n(x,t)}{\partial t} = -v_n(x,t)\frac{\partial n(x,t)}{\partial x} - n(x,t)\frac{\partial v_n(x,t)}{\partial x} + D_n\frac{\partial^2 n(x,t)}{\partial x^2} + \\ + \frac{\partial n(x,t)}{\partial x}\frac{\partial D_n(x,t)}{\partial x} + S_n\frac{\partial^2 T_C(x,t)}{\partial x^2} + \frac{\partial T_C(x)}{\partial x}\frac{\partial S_n(x)}{\partial x} \tag{3.5}$$

$$\frac{\partial p(x,t)}{\partial t} = -v_p(x,t)\frac{\partial p(x,t)}{\partial x} - p(x,t)\frac{\partial v_p(x,t)}{\partial x} + D_p\frac{\partial^2 p(x,t)}{\partial x^2} + \\ + \frac{\partial p(x,t)}{\partial x}\frac{\partial D_p(x,t)}{\partial x} + S_p\frac{\partial^2 T_C(x,t)}{\partial x^2} + \frac{\partial T_C(x)}{\partial x}\frac{\partial S_p(x)}{\partial x} \tag{3.6}$$

where $v_{n,p}(x)$ are the carrier velocities defined as:

$$\mathbf{v}_n = -\mu_n \mathbf{F} \tag{3.7}$$

$$\mathbf{v}_p = \mu_p \mathbf{F} \tag{3.8}$$

For the mobility we have adopted either of the two models decribed earlier. In particular, we have used the model 2.17 for fixed temperature simulations, and that of 2.19 when the time and/or space temperature variation has been accounted for. The discetization of 3.5 e 3.6 has been obtained with the following approximations for the spacial derivatives:

$$f_i' = \frac{1}{12\Delta x}(f_{i-2} - 8f_{i-1} + 8f_{i+1} - f_{i+2})$$

$$f_i'' = \frac{1}{12\Delta x^2}(-f_{i-2} + 16f_{i-1} - 30f_i + 16f_{i+1} - f_{i+2})$$

while for the time derivative a simpler discretization has been used:

$$\left(\frac{\partial n}{\partial t}\right)_i = \frac{1}{2\Delta t}(n_{i+1} + n_{i-1})$$

3.2.2 Poisson equation

During the simulation, it is necessary to upgrade the electric field value at fixed times, whose separation is determined by physical consideration (e.g. the plasma frequency of the carriers).
In one dimension, Poisson equation takes the form

$$\frac{\partial^2}{\partial x^2}\Phi(x) = -\frac{\rho(x)}{\epsilon} \tag{3.9}$$

where ϵ is the semiconductor dielectric constant and Φ the electrostatic potential, while the net charge ρ is given by

$$\rho(x) = -q[n(x) - p(x) - N_D^+ + N_A^-] \tag{3.10}$$

where q is the electron charge, N_A^- and N_D^+ are respectively the ionized acceptor and donor densities, and n e p are the free carrier (electron and hole) concentrations. The ionized donor (N_D^+) and acceptor (N_A^-) concentrations are given by

$$\begin{aligned} N_D^+ &= \frac{N_D}{1 + g_d exp\left(\frac{E_f - E_D}{K_b T}\right)} \\ N_A^- &= \frac{N_A}{1 + g_v exp\left(\frac{E_A - E_f}{K_b T}\right)} \end{aligned} \tag{3.11}$$

where E_f is the Fermi level, E_D and E_A the donor and acceptor energy, and $g_d = 2$, $g_v = 4$ their degeneracy factors.

Among the several ways to solve Poisson equation we have adopted the so-called "Gauss elimination" technique. We subdivide our 1D system into N cells (Poisson lattice), and discretize the equation:

$$\Phi_{i-1} - 2\Phi_i + \Phi_{i+1} = -\Delta x^2 \frac{\rho_i}{\epsilon} \tag{3.12}$$

where Δx is the fixed dimension of each cell. Boundary conditions are imposed on two extra cells, as shown in fig. 3.1

$$\begin{aligned} \Phi_0 &= V_{in} \\ \Phi_{N+1} &= V_{fin} \end{aligned}$$

V_{in} and V_{fin} being the bias levels. Let us consider the generalization of Eq. (3.12)

$$a_-\Phi_{i-1} + a\Phi_i + a_+\Phi_{i+1} = \rho_i' \tag{3.13}$$

and set

$$\Phi_{i+1} = \alpha_i \Phi_i + \beta_i \tag{3.14}$$

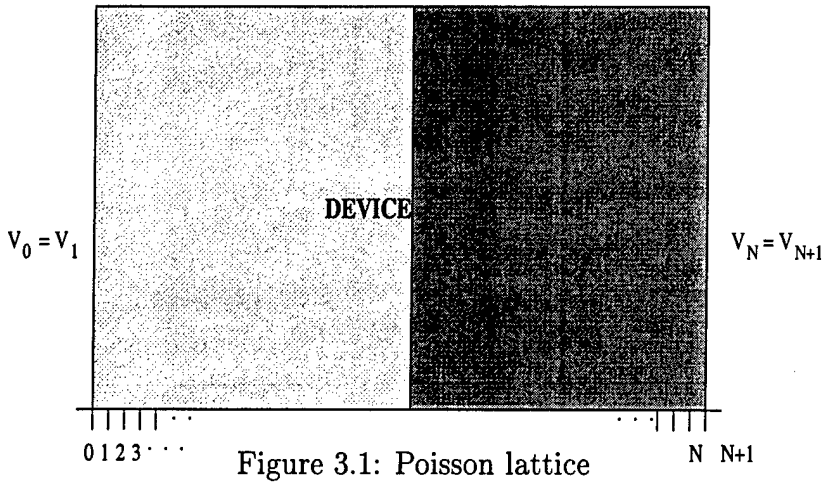

Figure 3.1: Poisson lattice

where α_i and β_i are constants. By substituting the previous expression into (3.13) we obtain:

$$\Phi_i = a - \gamma_i \Phi_{i-1} + \gamma_i (a_+ \beta_i - \rho_i') \tag{3.15}$$

with

$$\gamma_i = -\frac{1}{a + a_+ \alpha_i} \tag{3.16}$$

By comparing Eq. (3.15) with Eq. (3.13) the expression for the constant coefficients is found:

$$\begin{aligned} \alpha_{i-1} &= \gamma_i a_- \\ \beta_{i-1} &= \gamma_i (a_+ \beta_i - \rho_i') \end{aligned} \tag{3.17}$$

By imposing the first boundary condition

$$\Phi_{N+1} = V_{fin} = \alpha_N \Phi_N + \beta_N \tag{3.18}$$

we have

$$\begin{aligned} \alpha_N &= 0 \\ \beta_N &= V_{fin}. \end{aligned} \tag{3.19}$$

The method is now clear: starting from the condition (3.19) and using Eqs. (3.17) the α_i, β_i coefficients are determined. Using then the second boundary condition ($\Phi_0 = V_{in}$) Eq. (3.14) gives the potential values over the whole lattice.

In the special case of interest, that is the solution of Poisson equation:

$$\begin{aligned} a_- = a_+ &= 1 \\ a &= -2 \\ \rho_i' &= -(\Delta x)^2 \frac{\rho_i}{\epsilon} \end{aligned}$$

On scalar computers, the Gauss elimination method is much faster than matrix inversion approaches, as it requires N operation instead of N^2.
Once the electrostatic potential profile is calculated, the electric field is found from

$$F = -\frac{\partial \Phi}{\partial x} \tag{3.20}$$

which in the discrete version becomes:

$$F_i = -\frac{\Phi_{i-2} - 8\Phi_{i-1} + 8\Phi_{i+1} - \Phi_{i+2}}{12\Delta x}. \tag{3.21}$$

In order for the solution to have physical meaning, the parameters adopted in the numerical solution of any differential equation have to obey some constrains. For our case the mesh size has to be lower then the Debye length, given by:

$$L_D = \sqrt{\frac{ck_BT}{q^2N}}$$

where N is the doping.

The temporal time step has to be smaller of the dielectric relaxation time, given by :

$$t_{dr} = \frac{c}{qN\mu}.$$

3.2.3 Heat transport

The equation describing heat transpot (Eq. 3.4):

$$\rho c \frac{\partial T_C}{\partial t} - J \times F = \nabla \cdot (k(T_C)\nabla T_C) \tag{3.22}$$

can be discretized as follows (assuming a constant thermal conductivity k):

$$\frac{T_i^{m+1} - T_i^m}{\Delta t} = \frac{k}{\rho c}\left[\frac{-T_{i-2}^m + 16(T_{i-1^m} + T_{i+1}^m) - 30T_i^m - T_{i-2}^m}{12\Delta x(i)} + \frac{J_i^m * F_i^m}{k}\right]$$

$(i = 1, .., N)$,

from which the temperature in the i-th point at the $(m+1)$-th instant is found:

$$T_i^{m+1} = T_i^m + \frac{k * \Delta t}{\rho c}\left[\frac{-T_{i-2}^m + 16(T_{i-1}^m + T_{i+1}^m) - 30T_i^m - T_{i-2}^m}{12\Delta x(i)} + \frac{J_i^m * F_i^m}{k}\right]$$

$(i = 1, .., N)$,

where J_i^m and F_i^m are the total current density and the electric field in the i-th point. The boundary conditions are

$$T(-1) = T(0) = T(N+1) = T(N+2) = 300\,K$$

3.3 Generation processes

Two generation processes are important in our study: impact ionization and tunneling. As for the former process, in the absence of experimental values for the 4H politype, we will take the same values as for the 6H one. This assumption is justified by the fact that the breakdown voltages for PIN diodes obtained from the two materials are quite similar.

For the α-SiC, at room temperature impact ionization is caused preferably by holes. Since the valence band structure is similar[7], the same should occur in β-SiC. At higher temperatures, electrons also start contributing to the ionization, and a different behavior of the two politype has to be expected due to the differences in their conduction bands [7].

The total number of electron-hole pairs generated per unit time is

$$G_n = \frac{1}{q}(\alpha_n J_n + \alpha_p J_p)$$

where α_n and α_p are tensors, with

$$\alpha_{n\|} = \alpha_n, \qquad \alpha_{p\|} = \alpha_p$$

$$\alpha_{n\perp} = \alpha_n/3.5, \qquad \alpha_{p\perp} = \alpha_p$$

and

$$\alpha_{n,p}(E) = \alpha_{n,p} exp - \left(\frac{b_{n,p}}{E}\right).$$

On the basis of a fit with available experimental data, α_n and α_p have the following dependence on temperature:

$$\alpha_n(T) = 7.628 \times 10^6 (T/300)^2 + 1.506 \times 10^6 (T/300) - 4.184 \times 10^6 [cm^{-1}]$$

$$\alpha_p(T) = 1.469 \times 10^6 (T/300)^2 + 1.083 \times 10^7 (T/300) - 3.100 \times 10^7 [cm^{-1}]$$

$b_n(T) = 2.58 \times 10^6$ [V/cm] (indipendent of T)
$b_p(T) = 1.90 \times 10^7$ [V/cm] (indipendent of T)[7].

As for the tunneling contribution (G_n and G_n for electrons and holes, respectively) we have used the following model:

$$G_{n,p} = \frac{n_{d,a}}{\tau_{n,p}}$$

$$\tau_{n,p}^{-1} = \omega_{n,p} \frac{\alpha_{n,p}}{F} e^{\left(-\frac{\alpha_{n,p}}{F}\right)}$$

$$\alpha_{n,p} = \frac{4E_{d,a}^{\frac{3}{2}}\sqrt{2m_{n,p}^{*}}}{3eh}$$

$$\omega_{n,p} = \frac{12E_{d,a}}{\hbar}$$

The quantities n_d and n_a are the concentration of unionized dopants, calculated at the j-th time step as:

$$n_{d,ai}^{j} = n_{d,a0i} e^{-\sum_{0}^{j} \frac{j\Delta t}{\tau_{n,pi}^{j}}}$$

3.4 Basic structure of the simulated N^+NP^+ diode

The structure of the simulated diode is shown in Fig. 3.2. The diode is made up by a 0.25 μm wide N-region (doped at $5^{18} cm^{-3}$), followed by a second N-type region of 0.6 μm doped at $10^{18}\, cm^{-3}$.

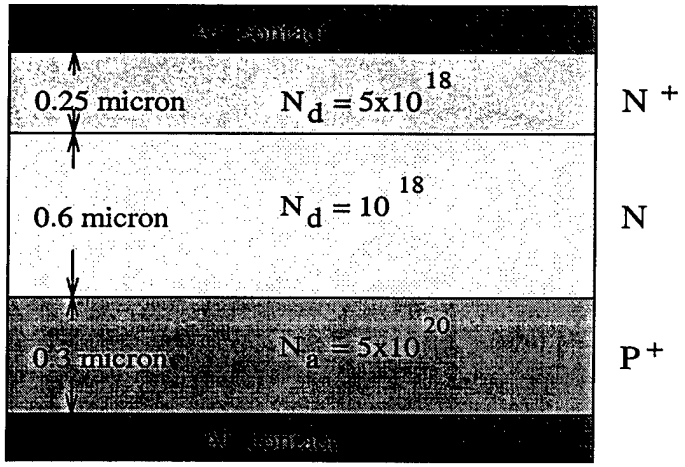

Figure 3.2: *Simulated diode structure*

The third region is p-type, with a density of 5^{20},cm^{-3} and a width of 0.3 μm. The contacts on the heavily doped n and p regiona are made of Aluminum.

The dimension and doping levels of the device have strong influence on the simulation. In fact, in order to have a sufficient number of mesh points a spacial mesh $\Delta x = 10^{-9}$m has been taken, which has in turn implied a large number of discretization points and a heavy computational load.
Furthermore, in order to guarantee the stability of the finite difference algorithm, the Von Neumann criterion requires that

$$\frac{v\Delta t}{\Delta x} < 1.$$

Since the saturation velocity in SiC is $2 \times 10^7 cm/s$, a value $\Delta t < 5 \times 10^{-14} s$ is needed. Actually, an even smaller time step is requires by the fact that tunneling times as short as 5×10^{-14} are calculated in the high field region of the device, which forced us to use time steps of the order of 2×10^{-16}, thus increasing enormously the complexity of the numerical algorithm. In order to speed up the simulation under transient conditions, the depletion approximation for each junction is used as initial condition to each simulation.

3.5 Simulation parameters

The following table (tab. 3.1) illustrates the parameters used in the simulation of 6H e 4H-SiC diodes.

Table 3.1: Simulation parameters

	$6H$	$4H$
Dielet.const.ϵ	9.66	9.66
Energy gap	$E_g = 2.86eV$	$E_g = 3.2eV$
Electron mass	$m_{n0} = 0.41$	$m_{n0} = 0.41$
Hole mass	$m_{p0} = 1$	$m_{p0} = 1$
Acceptor level	$E_A = 0.2eV$	$E_A = 0.191eV$
Donor level	$E_D = 0.1eV$	$E_D = 0.065eV$
Ioniz. const.	$g_c = 2$ $g_v = 4$	$g_c = 2$ $g_v = 4$
Mobility (300K)		
(cm^2/Vs)	$\mu_n^{min} = 20$ $\mu_p^{min} = 5$ $\mu_n^{delta} = 380$ $\mu_p^{delta} = 70$	$\mu_n^{min} = 20$ $\mu_n^{min} = 5$ $\mu_n^{delta} = 380$ $\mu_n^{delta} = 70$
(cm^{-3})	$N_n^{\mu} = 4.5 \times 10^{17}$ $N_p^{\mu} = 1 \times 10^{19}$	$N_n^{\mu} = 4.5 \times 10^{17}$ $N_p^{\mu} = 1 \times 10^{19}$

	$6H$	$4H$
	$\alpha_n = -3$ $\alpha_p = -3$	$\alpha_n = -3$ $\alpha_p = -3$
	$\gamma_n = 0.45$ $\gamma_p = 0.5$	$\gamma_n = 0.45$ $\gamma_p = 0.5$
	$\beta_n = 2$	$\beta_n = 2$
Sat. vel. (cm/s)	$v_{n,s} = 2 \times 10^7$ $v_{p,s} = 2 \times 10^7$	$v_{n,s} = 2 \times 10^7$ $v_{p,s} = 2 \times 10^7$
Impact ionization		
(cm^{-1})	$a_n = 1.66 \times 10^6$ $a_p = 5.18 \times 10^6$	$a_n = 1.66 \times 10^6$ $a_p = 5.18 \times 10^6$
(V/cm)	$b_n = 1.273 \times 10^7$ $b_p = 1.4 \times 10^7$	$b_n = 1.273 \times 10^7$ $b_p = 1.4 \times 10^7$
Thermal cond. W/cmK	$K = 4.9$	$K = 4.9$

Chapter 4

Diode simulation

As a first step for the simulation, we have verified that the models provides realistic profiles under "normal" conditions. For instance, we have biased the diode under reverse voltage and checked the with of the depletion region with respect to analitical results. Once the physical model and the numerical algorithm have proven to be correct, we have started a series of simulation of the time dependent response of SiC diodes to a voltage step. Due to the heavy computational load, we have not been able to apply rising times and pulse of ns duration, as in the experiment of Fazi and Neudeck. Rather, we have simulated rise times of the order of a ps, and we have looked at the diode dynamics toward the steady state condition.

4.0.1 Diode response in the absence of field-assisted ionization and impact ionization

In figs. 4.1(a) and (b) we show the time evolution of the applied voltage ($V_{b.in} - V_{app}$) and of the electron current density J_n. The application of a reverse voltage step of $100V$ over 1 ps (from t=4ps up to t=5ps)generates a current pulse due to the carrier movement following the sudden change of the electric field. At the end of such transient, the current goes back to zero, as expected under steady reverse bias in the presence only of thermal effects.

In fig.4.2 we see that the electric field evolves towards a steady state value much higher than that reached at the end of the voltage step. Thus, the transient does not lead to an overshoot in the field peak value, as it might have been expected. The dynamics of the carrier concentratio (Fig. 4.3) is consistent with the electric field one, showing the large depletion region reached in steady state.

4.0.2 Diode response in the presence of tunneling or impact ionization

When tunneling is considered, the current response has the same shape as seen before (Fig.4.4), but the peak value is much higher. This is due to the fact that the high field values reached while approaching stationary conditions lead to sizeable carrier tunneling out of donor and acceptor states. This is confirmed by the distributions

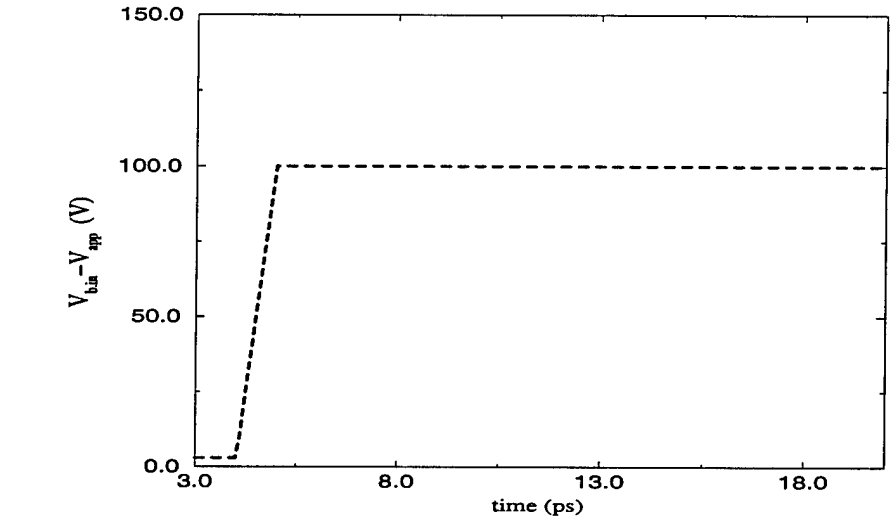

(a)

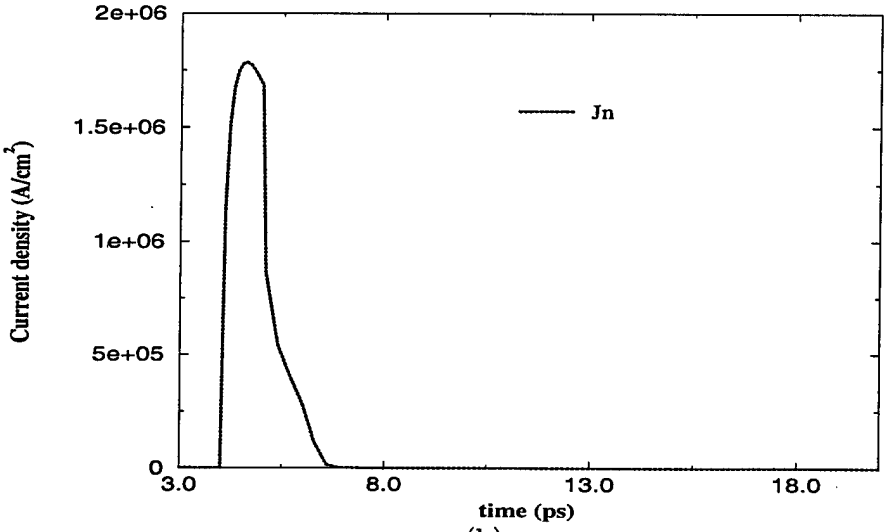

(b)

Figure 4.1: *(a):Applied bias; (b): Current response without tunneling and ionization*

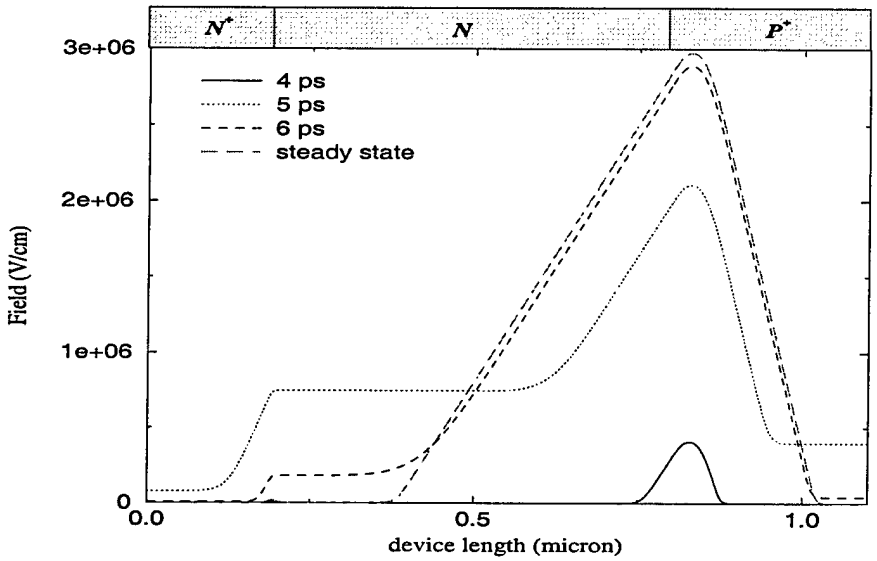

Figure 4.2: *Electric field evolution*

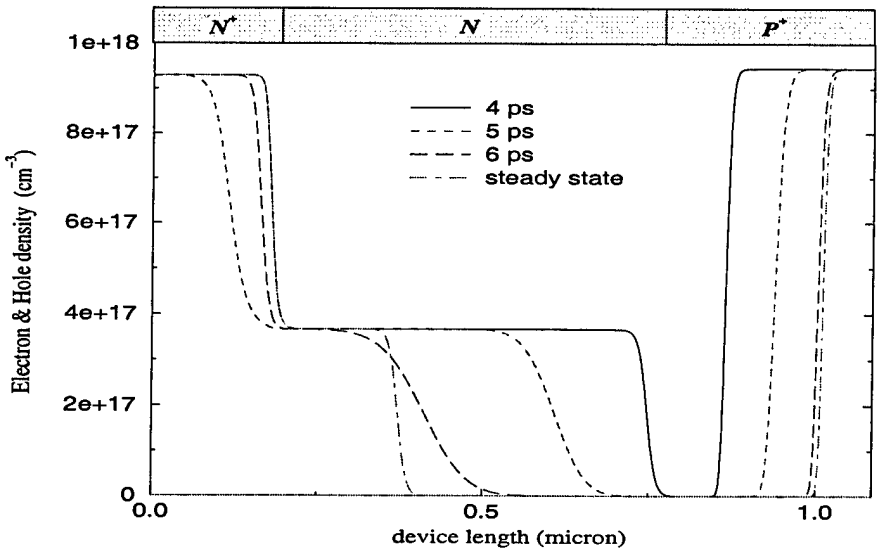

Figure 4.3: *Carrier evolution during transient*

of carriers, unionized donors and acceptors (fig.4.7). At the end of the voltage step, all donors in the N region are completely ionized, while in the N^+ and P^+ the complete ionization condition is not reached. The net result is that the electron and hole concentration are respectively a factor two and three than in the absence of tunneling.

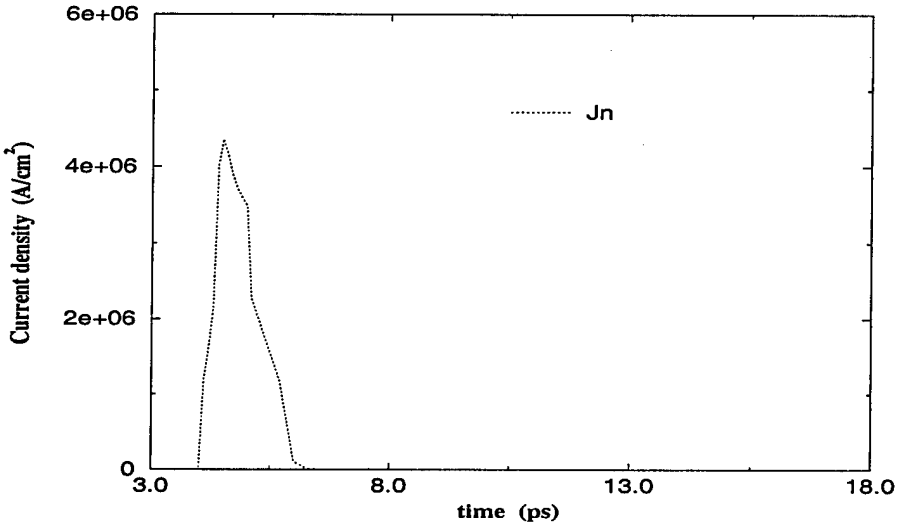

Figure 4.4: *Current response in the presence of tunneling*

As a consequence of the increased amount of free and fixed charges, the electric field values are also higher (the maximum field grows from $3 \times 10^6\ V/cm$ to $5.5 \times 10^6\ V/cm$). From the time evolution of the various quantities, it can be noticed that the tunneling process is very fast, as espected from the large value of the corresponding rates.

¿From Fig. 4.7 we notice the complete donor ionization in the n layer, and the only partial ionization of the dopants in the highly doped regions.
The electron density profile at the N^+N displays at very short time an interesting feature. As the electrons are injected in the *N-zone*, they experience a strong acceleration towards the N^+ region caused by the strong electric field of the depleted zone. As they reach the interface, the electric field abruptly drops and the electrons slow down, leading to the accumulation layer visible in the picture. In order to check if such short-time effect still exists when the rise time of the voltage step is longer, we have simulated a single voltage step of $100V$ with a rise time of 100 ps starting from t=0.

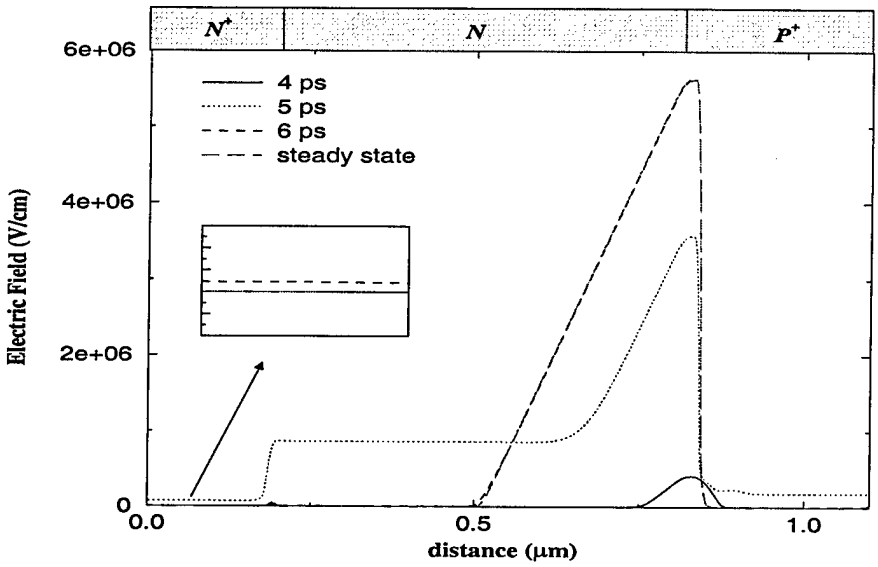

Figure 4.5: *Electric field evolution in the presence of tunneling*

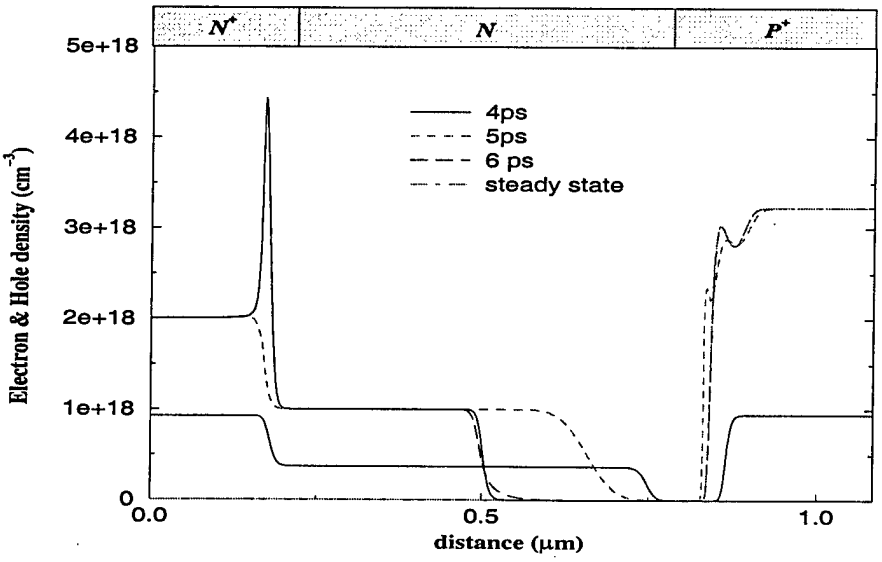

Figure 4.6: *Carrier concentration in the presence of tunneling*

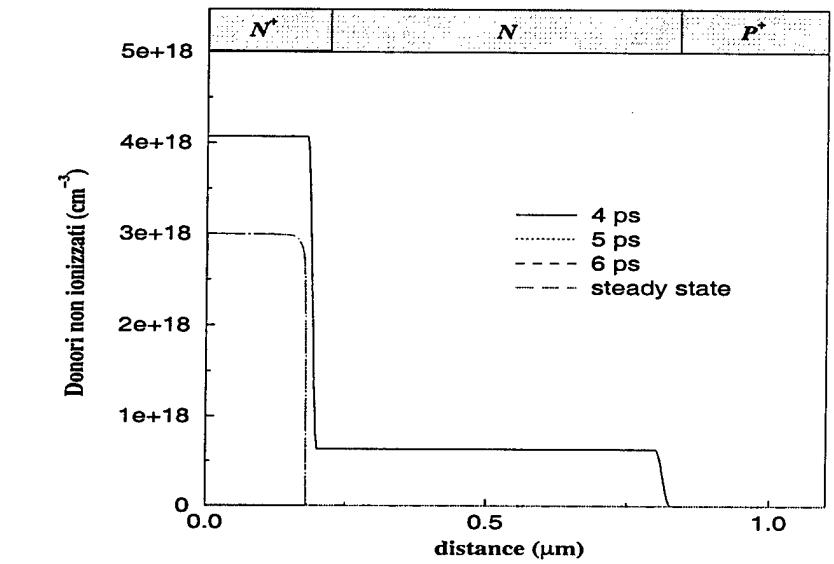

(a)

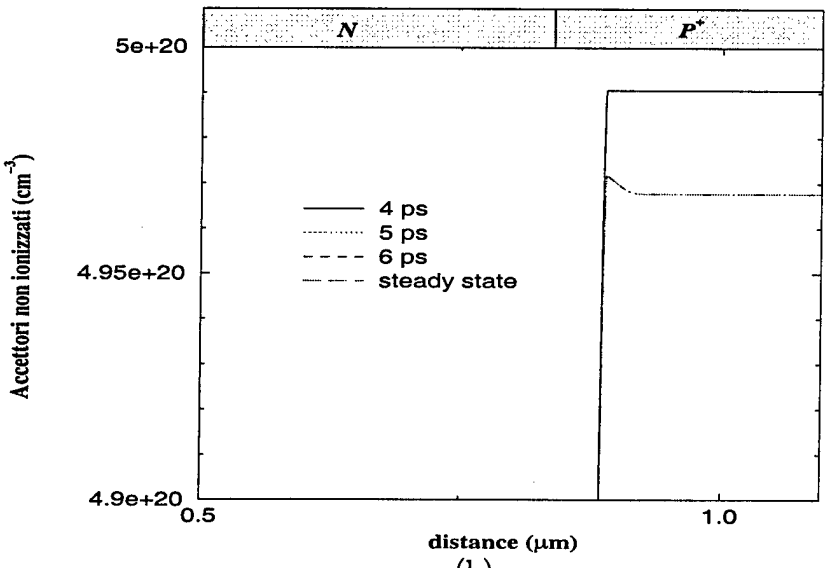

(b)

Figure 4.7: *Unionized donor (a) and acceptor (b) concentration in the presence of tunneling*

Figs.4.8,4.9,4.10 show the temporal evolution of the current, carrier concentration, and electric field, respectively, indicating the the electron acculation found previously was due to the ultrashort rise time. In steady state, very similar results are found.

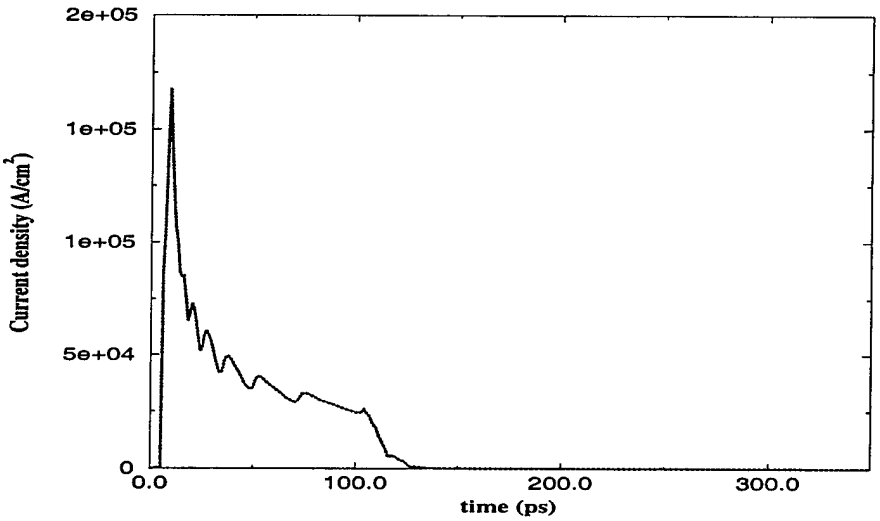

Figure 4.8: *Current evolution for a rise time* $t_{rise} = 100\,ps$ *(tunneling only)*

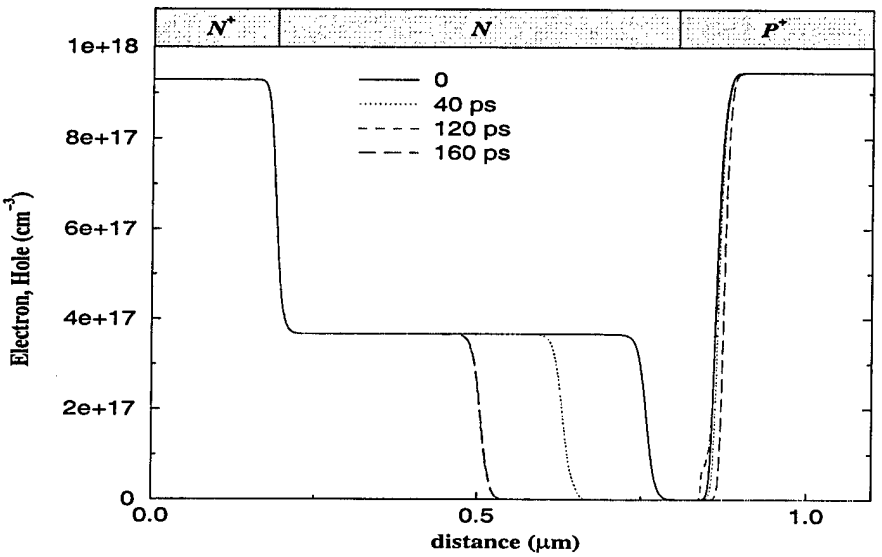

Figure 4.9: *Carrier concentration evolution for* $t_{rise} = 100\,ps$ *(tunneling only)*

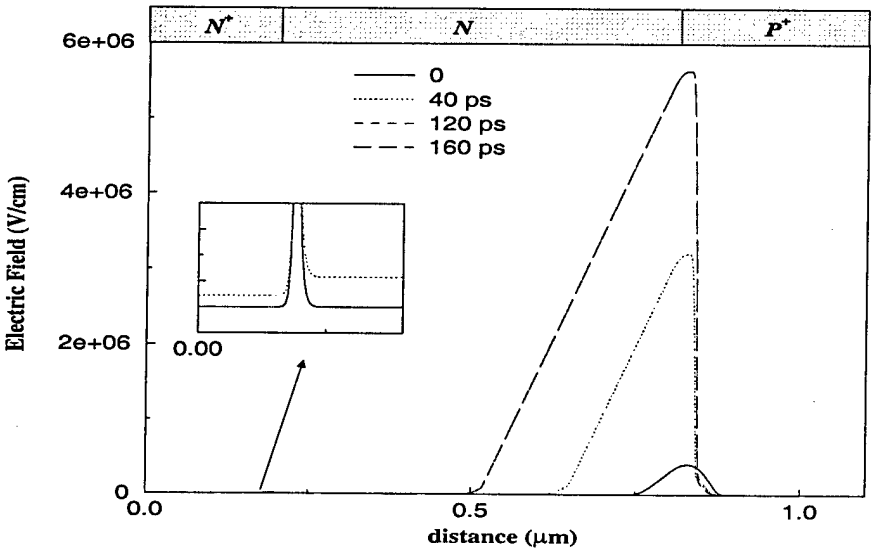

Figure 4.10: *Electric field evolution for* $t_{rise} = 100\,ps$ *(tunneling only)*

When only impact ionization is considered, no appreciable different is found with respect to the case of no ionization. That is, the electric field is always below the threshold value for such process. As a result, the current goes to zero after the initial transient (fig.4.11).

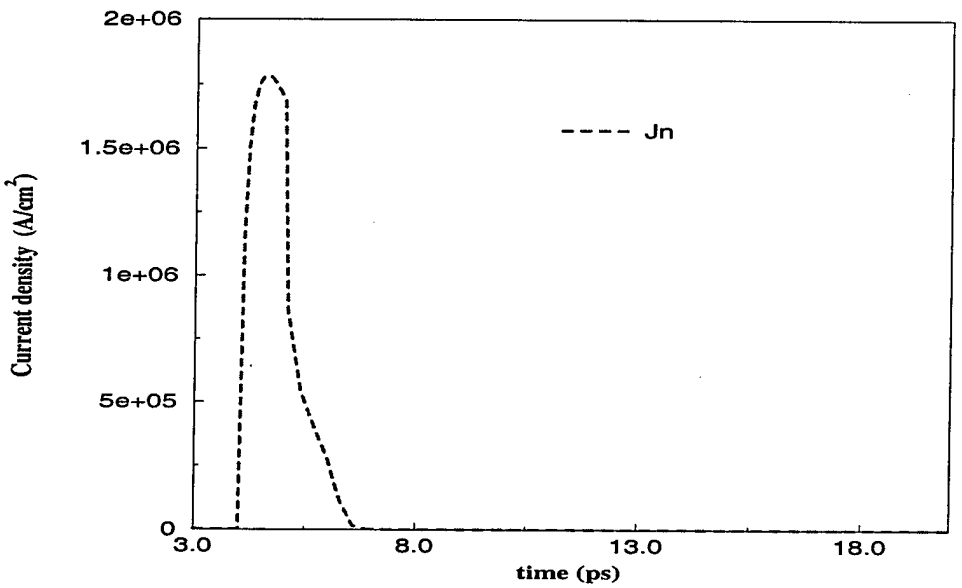

Figure 4.11: *Corrente in the presence of impact ionization* ($V_{b.in} - V_{app} = 100V$)

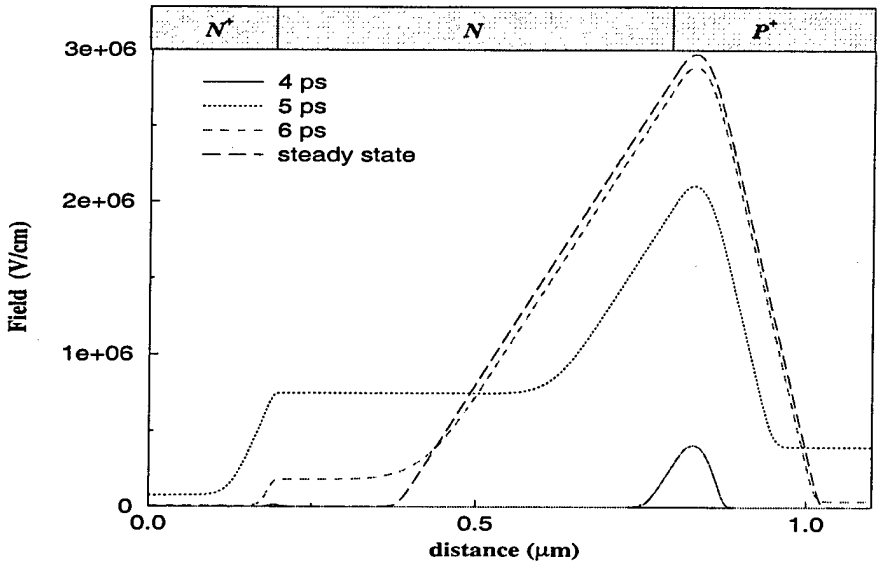

Figure 4.12: *Electric field in the presence of impact ionization* ($V_{b.in} - V_{app} = 100V$)

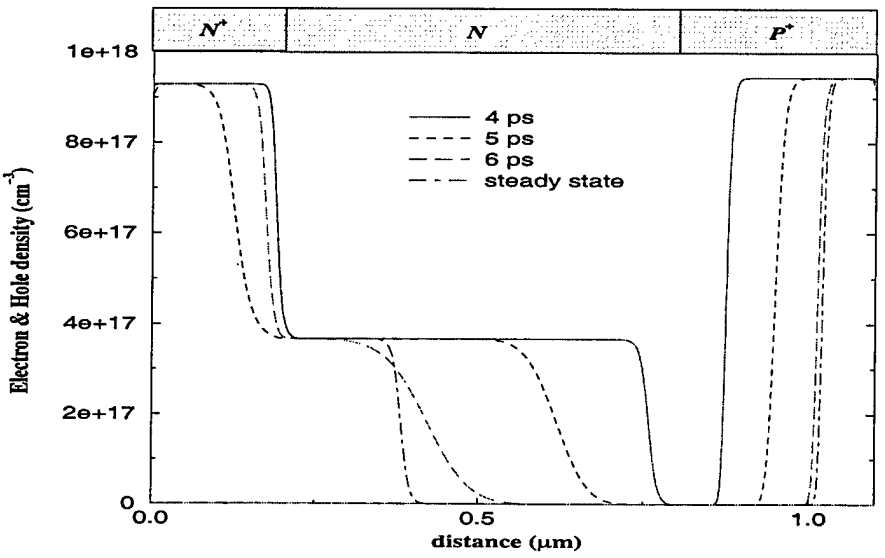

Figure 4.13: *Carrier concentration in the presence of impact ionization* ($V_{b.in} - V_{app} = 100V$)

Figure 4.14 shows that a non vanish (starting at T=4ps) steady current is obtained when a bias of $170\,V$ is applied with a rise time of $2\,ps$. Thus, the contribution of impact ionization to the persistent current is actually a function of the value and slope of the initial potential step.

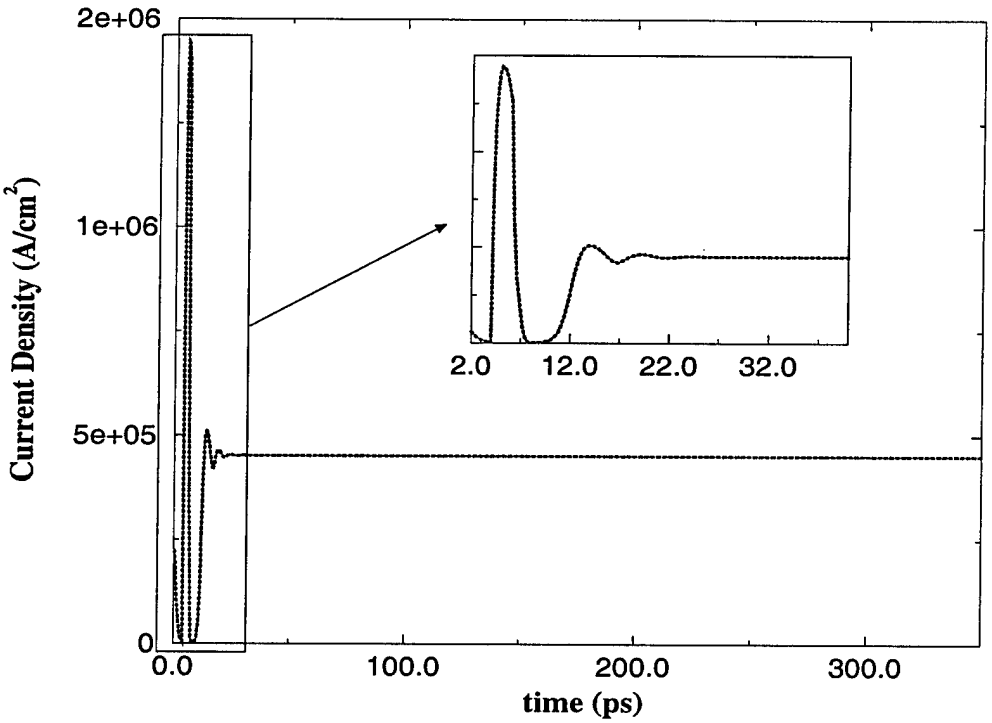

Figure 4.14: *Current density in the presence of impact ionization* ($V_{b.in} - V_{app} = 170\,V$)

Dynamically, we can see that while the current tends to return to zero, ionization processes start that push the current value up to its stationary value. The profiles of carrier concentration (figs.4.16 and 4.17 indicate that significant ionization (and the corresponding widening of the depletion region) initiates around $1\,ps$ after the step. The electric field displays an enhancement in the N region and a decrease in both N^+ e P^+ zones during the initial current pulse, followed by a reversed behavior when impact ionization start contributing. From figs.4.18 (a,b) we can see that indeed the ionization rate achieves its maximum value after $12\,ps$.

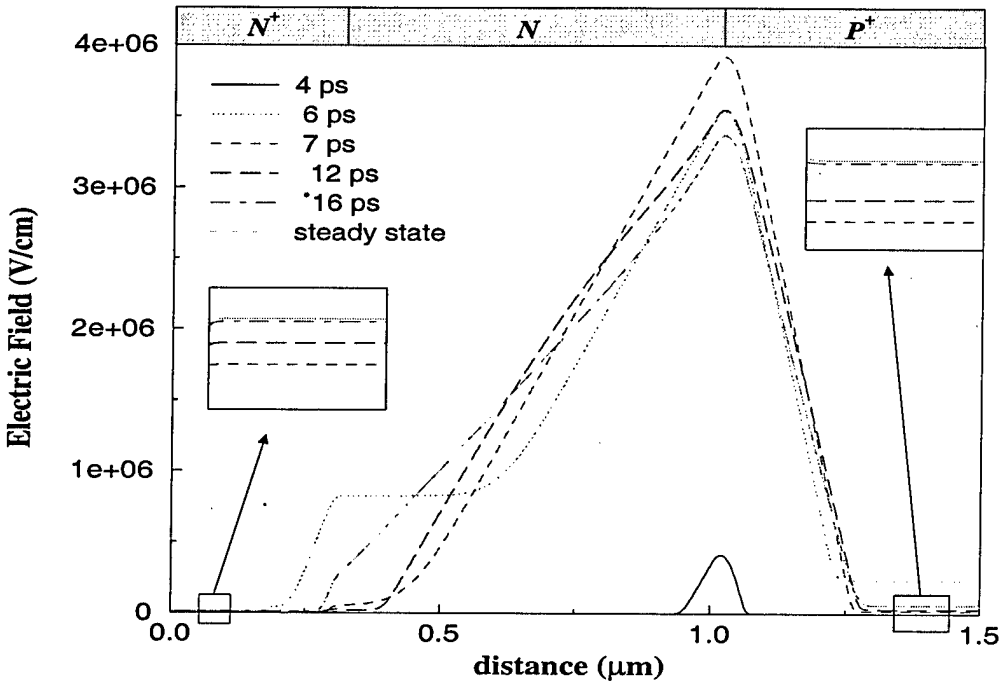

Figure 4.15: *Electric field in the presence of impact ionization* ($V_{b.in} - V_{app} = 170\,V$)

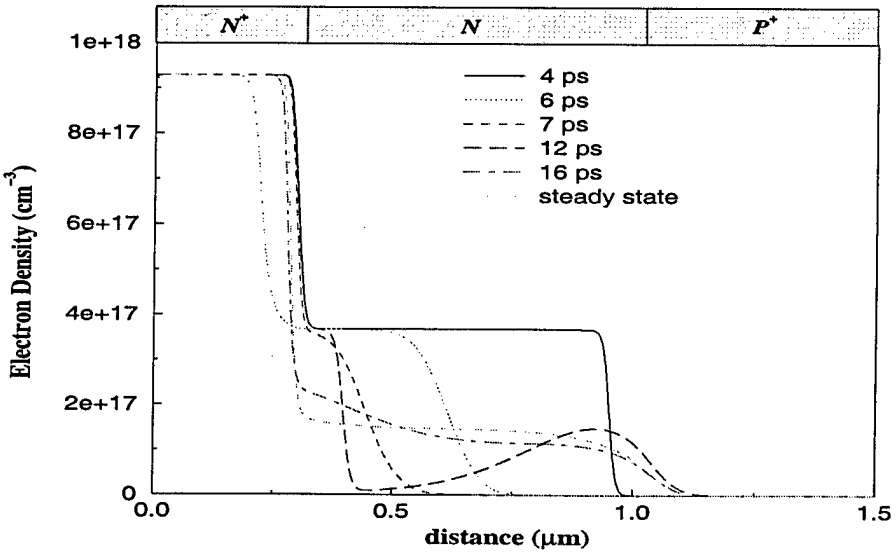

Figure 4.16: *Electron concentration in the presence of impact ionization* ($V_{b.in} - V_{app} = 170\,V$)

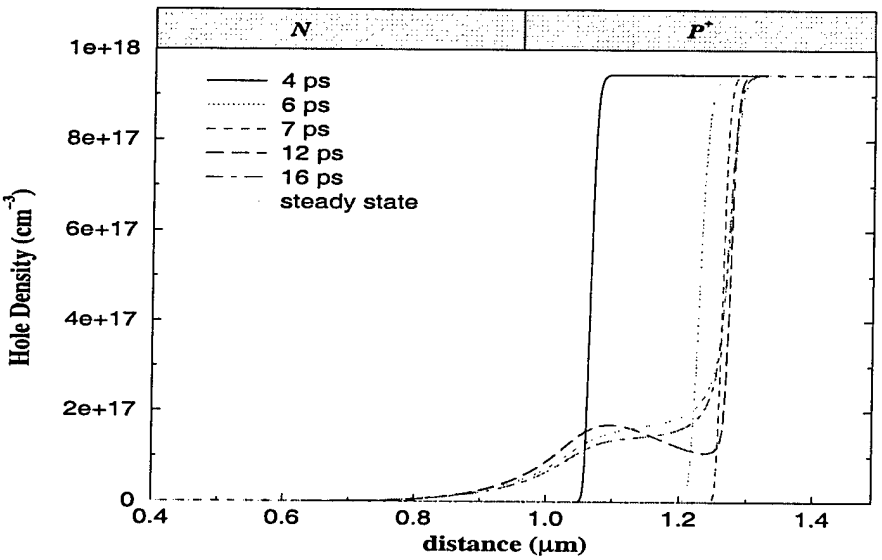

Figure 4.17: *Hole concentration in the presence of impact ionization* ($V_{b.in} - V_{app} = 170\,V$)

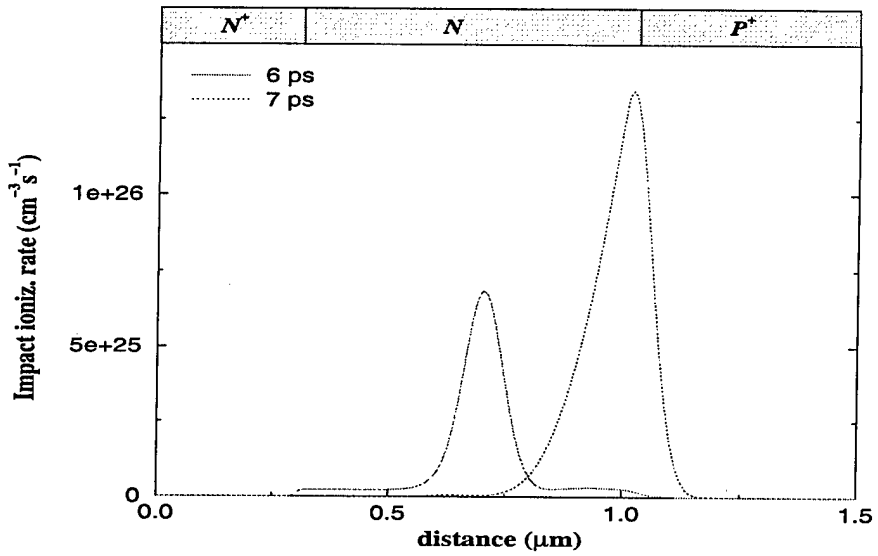

(a)

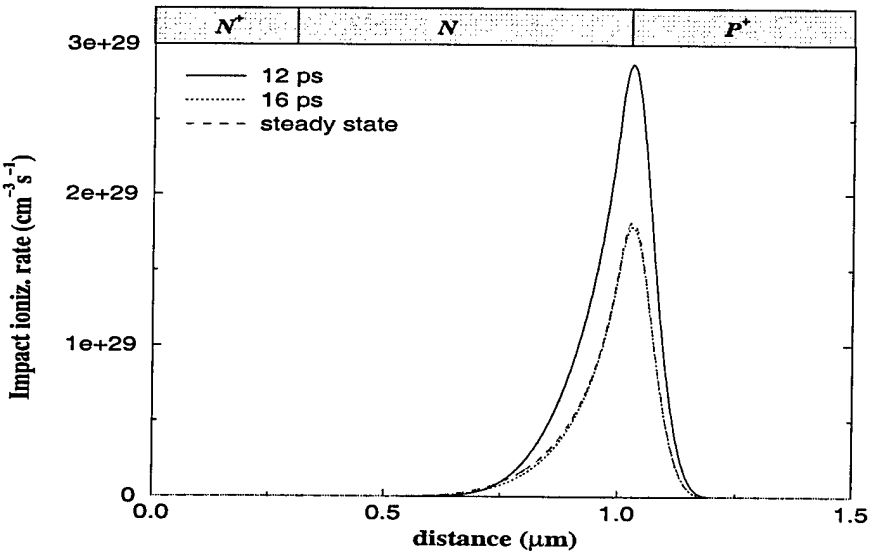

(b)

Figure 4.18: *Impact ionization rate* ($V_{b.in} - V_{app} = 170\,V$)

4.0.3 Response in the presence of tunneling and impact ionization

When both tunneling and ionization are present, a finite stationary current is found, in agreement with the experimental findings. The current shows an oscillatory behavior in response to the step potential, but does not return to zero as it is substained by a continious generation of carriers which eventually leads to the disappearence of the depletion region.

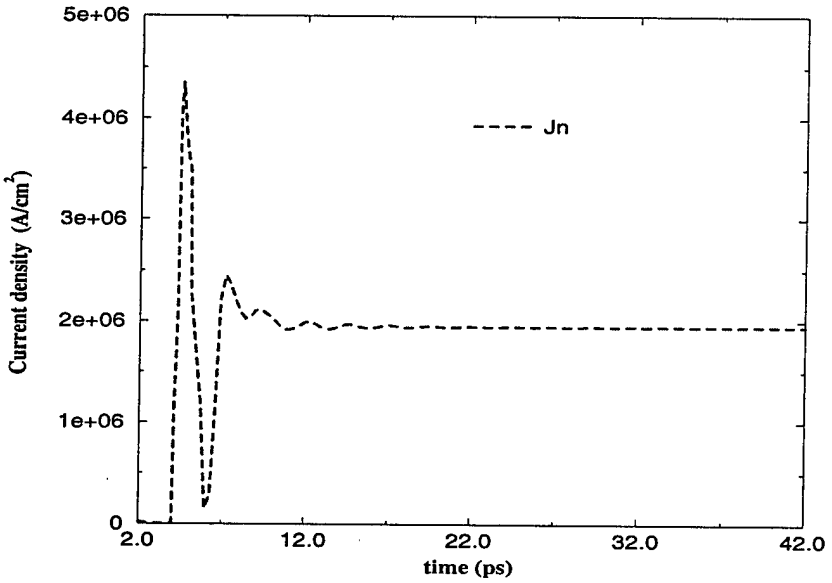

Figure 4.19: *Current density in the presence of tunneling and ionization*

At the end of the pulse, the ionization rate is fairly low, but it grows steadily with time as the electric field increases. In the proximity of the junction the field is actually so high to give almost complete ionization of the dopants.

In figs.4.19,4.20,4.21,4.23 the temporal evolution of electric field, carrier concentration, and depletion charge is reported. Near the $N - P^+$ the hole concentration presents a peak due to the large contribution of impact ionization processes caused by the junction field.

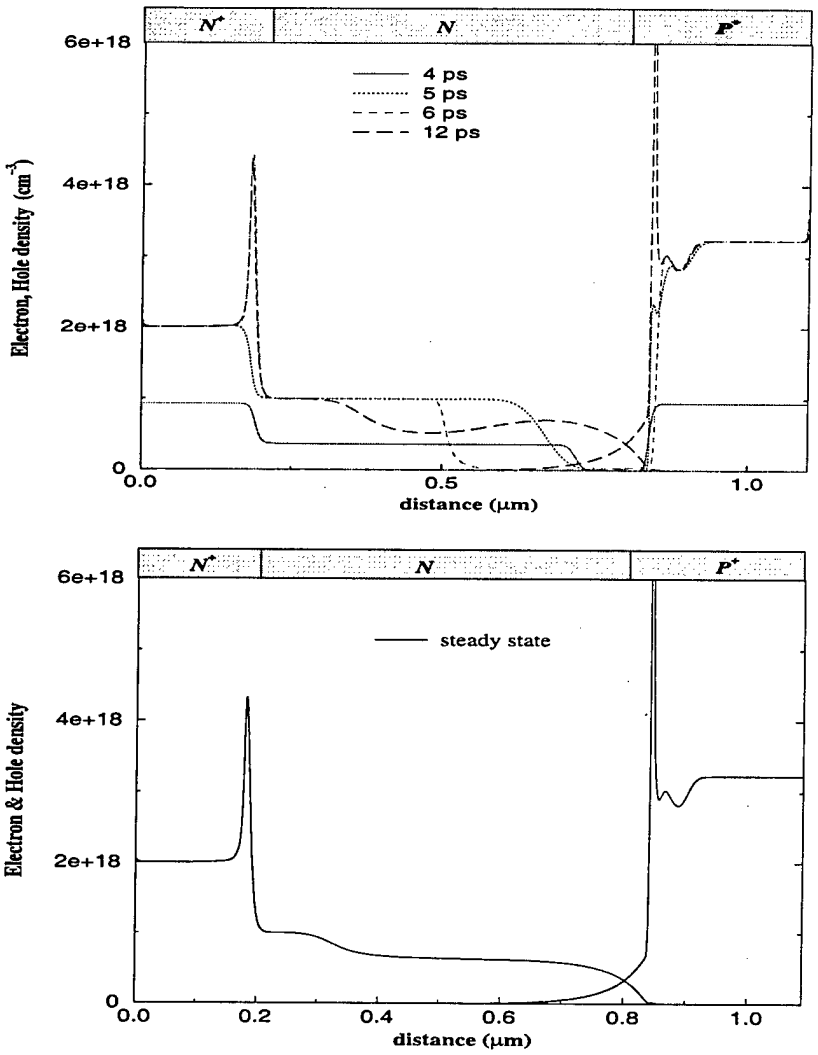

Figure 4.20: *Carrier concentration in the presence of tunneling and ionization*

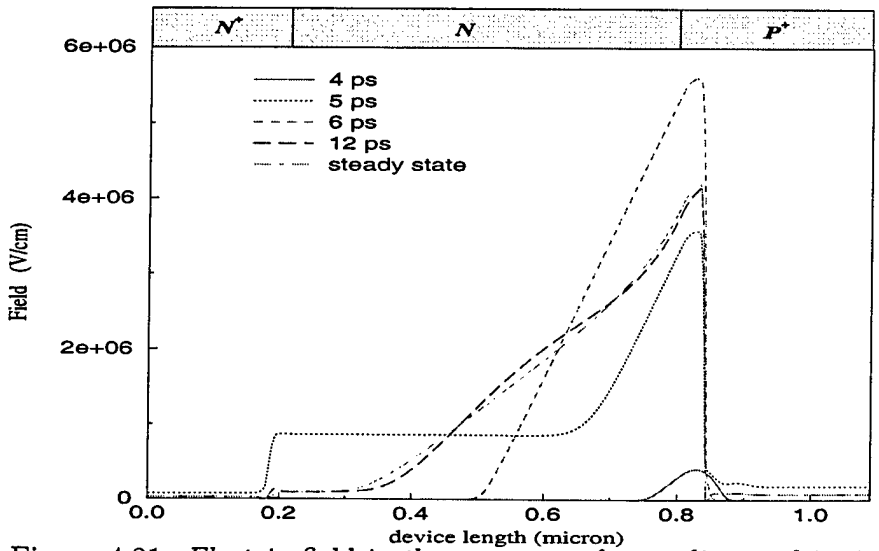

Figure 4.21: *Electric field in the presence of tunneling and ionization*

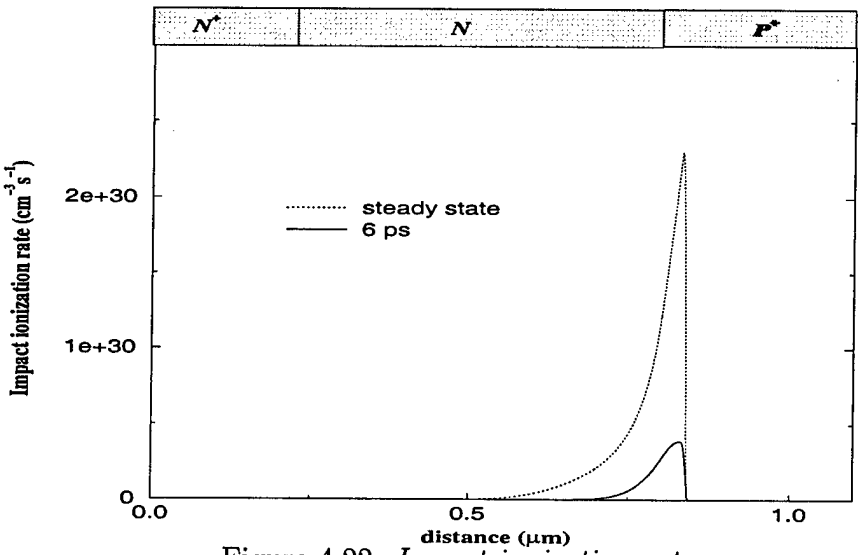

Figure 4.22: *Impact ionization rate*

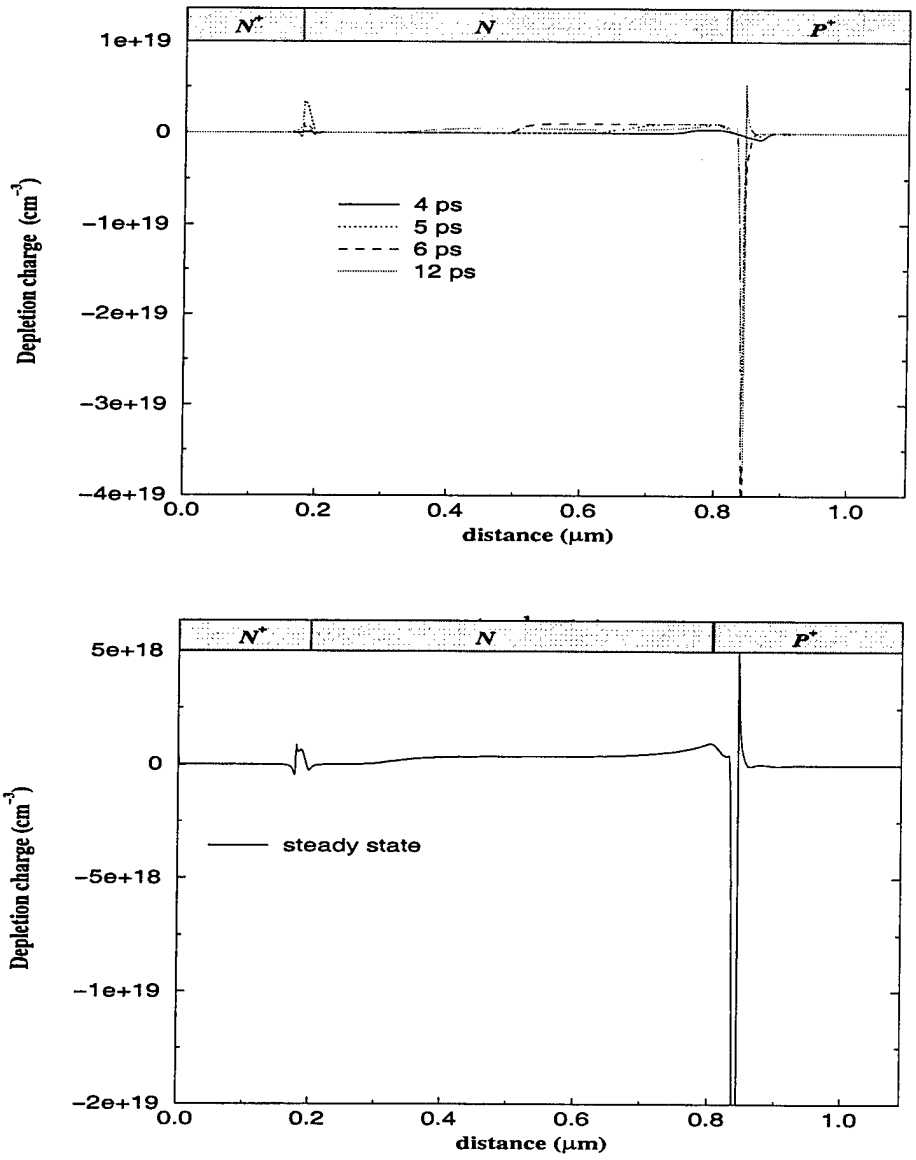

Figure 4.23: *Fixed charge in the presence of tunneling and ionization*

4.0.4 Influence of deep levels

We have also studied the influence of deep levels on the electrical response of SiC N^+NP^+ diode. The doping levels and the width of each region are respectively 5×10^{18}, 10^{18}, 5×10^{20} cm^{-3} and 0.2, 0.6 e $0.3\mu m$. A rise time of $100\,ps$ has been considered.
Figure 4.24 (dashed line shows the current behavior for donor and acceptor levels respectively at $E_D = 100\,meV$, $E_A = 600\,meV$. Only impact ionization processes are considered. The initial current spike is due to a displacement contribution. The current then raises further as the internal electric field grows towards the cathod, leading to a rather weak generation of holes. Most acceptors remain unionized. The slow current rise reflects well the experimental findings, indicating that deep acceptor levels do indeed contribute to the conduction mechanisms.

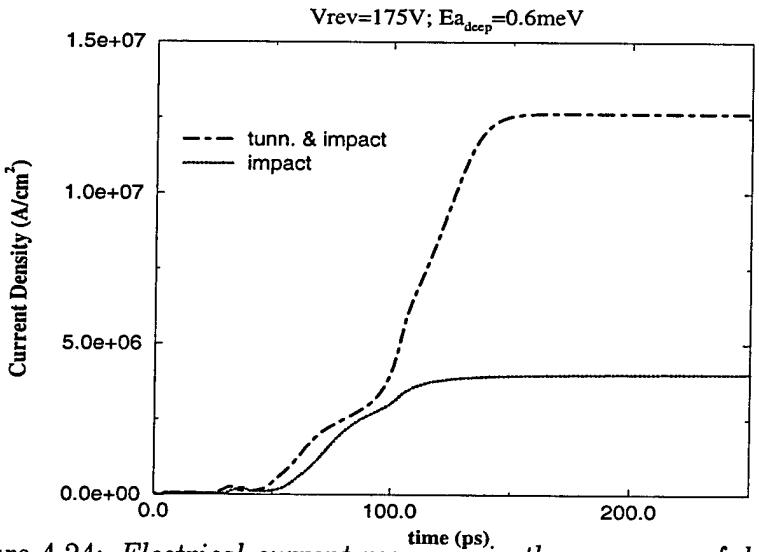

Figure 4.24: *Electrical current response in the presence of deep levels*

When tunneling is also considered, the current does not tend to saturate but inreases further, up to values a factor three higher than in the absence of tunneling processes. Such enhancement is directly related to the increased number of free carriers and ionized acceptors (see fig.4.24) in the device, favoured by the high electric field at the edge of the N^+ and P^+ zones.

4.0.5 Internal heating effects

We have perviously described the simplified model that allows us to account for the temperature variation connected to the current flux inside the diode, and to calculate its profile. The algorithm that we have implementented gives us directly the temperature map inside the device at every time step, thus providing information on the influence of internal heating on the dynamical response to the voltage pulses. A temperature-dependent mobility model is used to update constantly the carrier

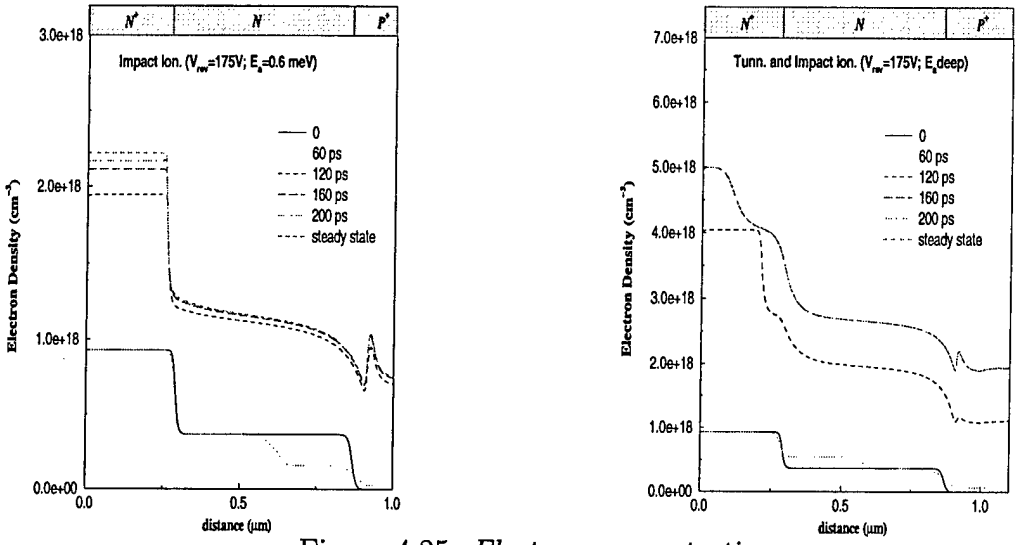

Figure 4.25: *Electron concentration*

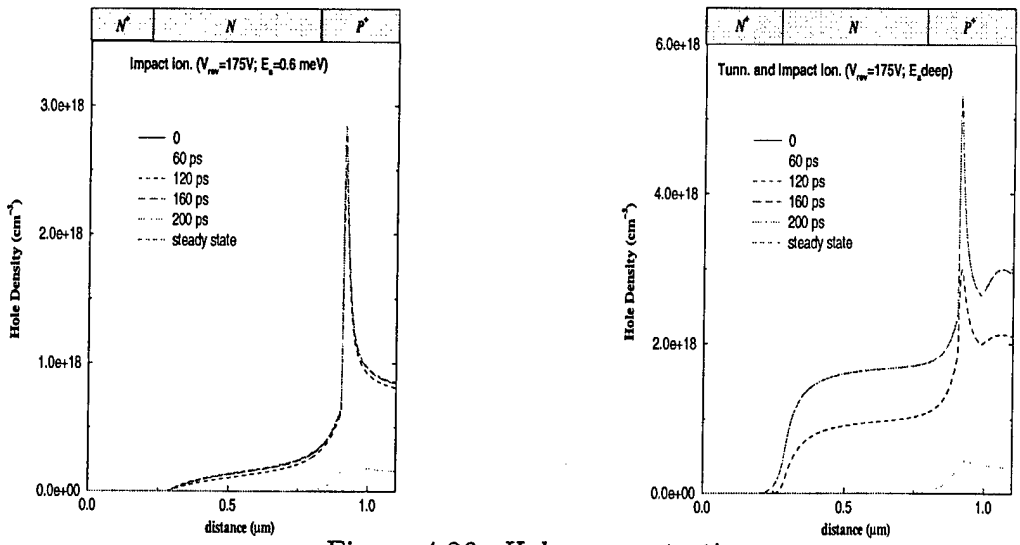

Figure 4.26: *Hole concentration*

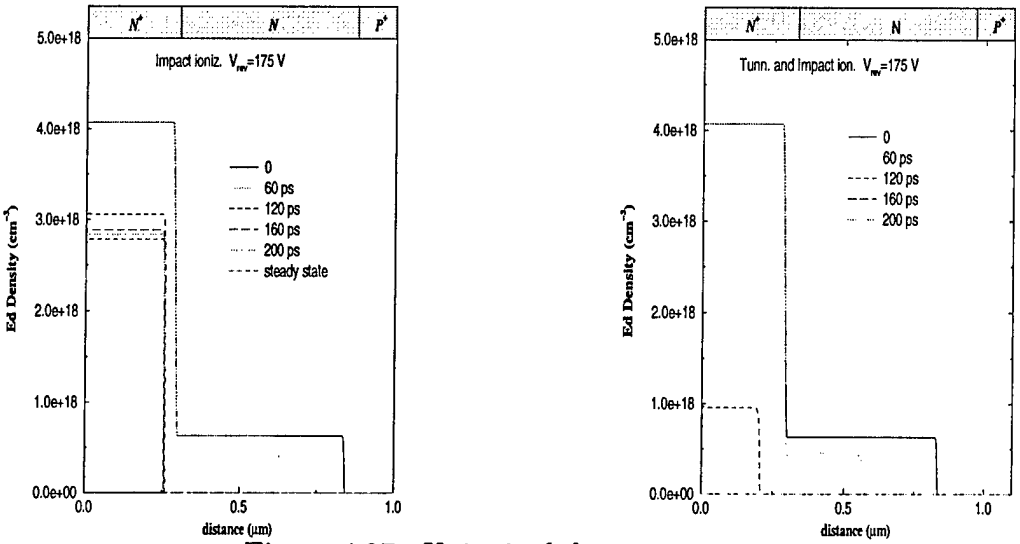

Figure 4.27: *Unionized donor concentration*

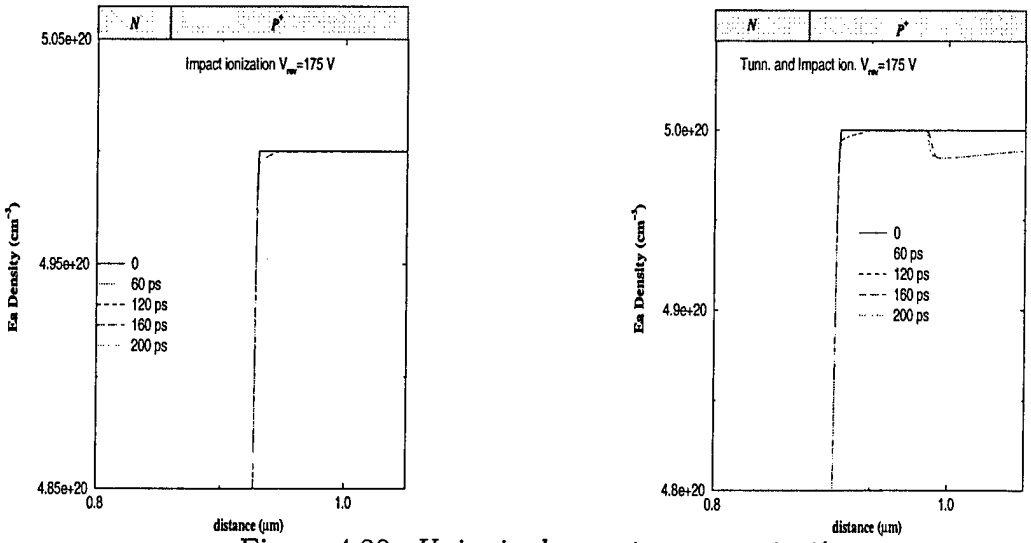

Figure 4.28: *Unionized acceptor concentration*

mobility to the changing temperature. In the simulation a voltage step of $100\,V$ has been considered with a rise time of $1\,ps$(starting at 4ps).

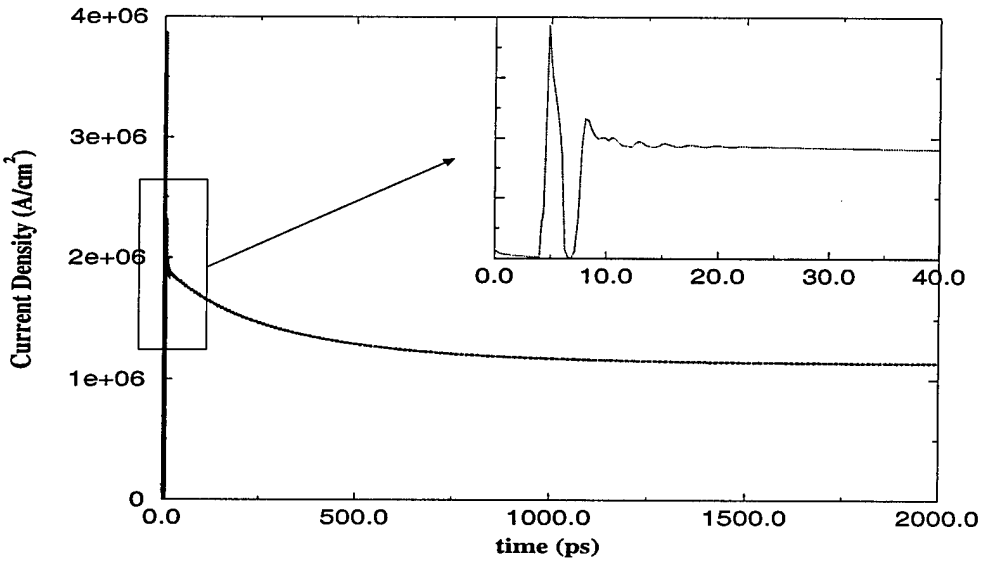

Figure 4.29: *Electrical current in the presence of self heating*

Figures 4.29 and 4.30 show respectively the evolution of the electrical current and of the internal temperature. Clearly, the temperature reacts much slower than the current to the voltage pulse, a consequence of the longer characteristic times for heat conduction.

The effect of the increasing temperature can be seen from figs.4.32 and figg.4.33 e 4.34, showing respectively the carrier concentration and drift velocity, for both electrons and holes. The temperature increase causes a reduction in time of the carrier mobility and drift velocity. The carrier concentration in the doped contact regions increases due to the higher thermal ionization of the dopants.

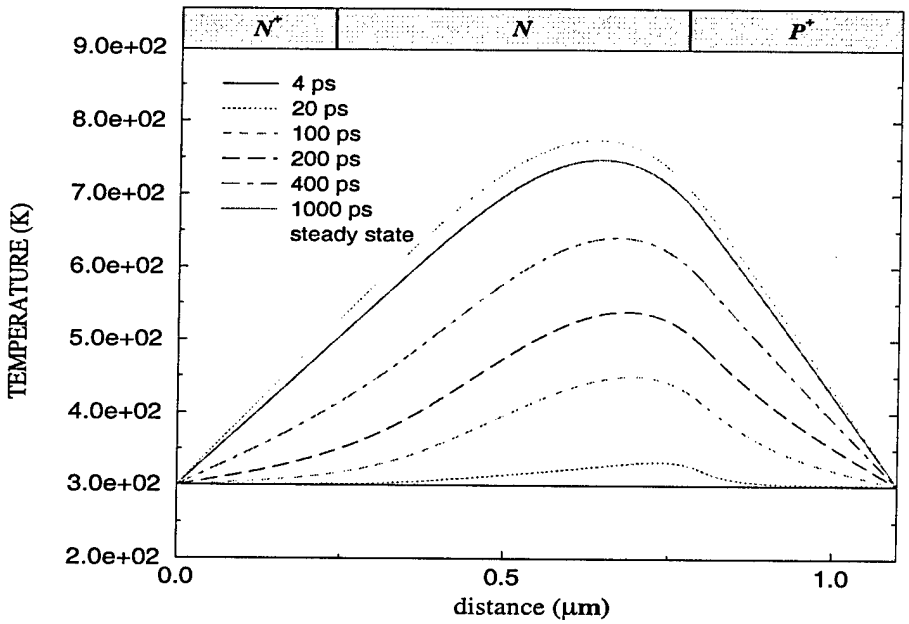

Figure 4.30: *Time evolution of the internal temperature during the current transient*

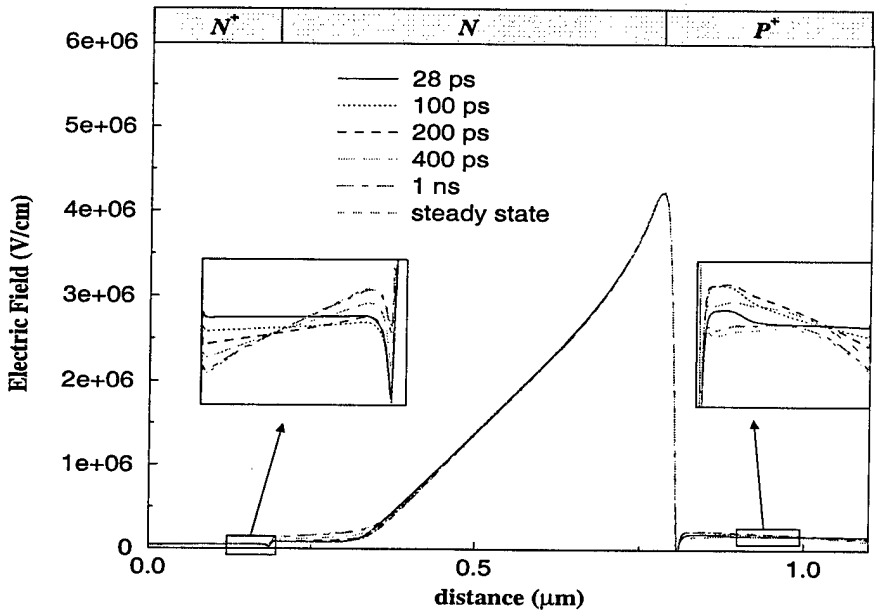

Figure 4.31: *Electric field evolution*

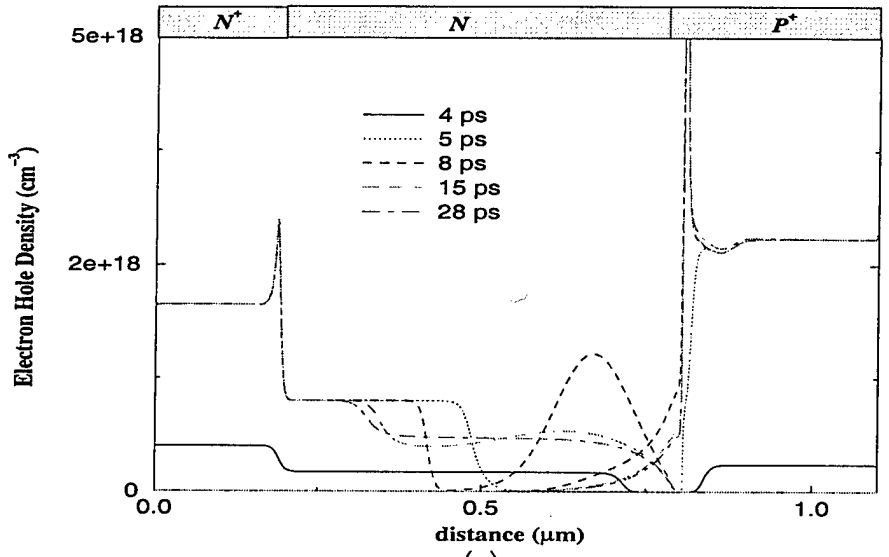

Figure 4.32: *(a) Transient evolution of the carrier concentration; (b) Approach to the stationary condition*

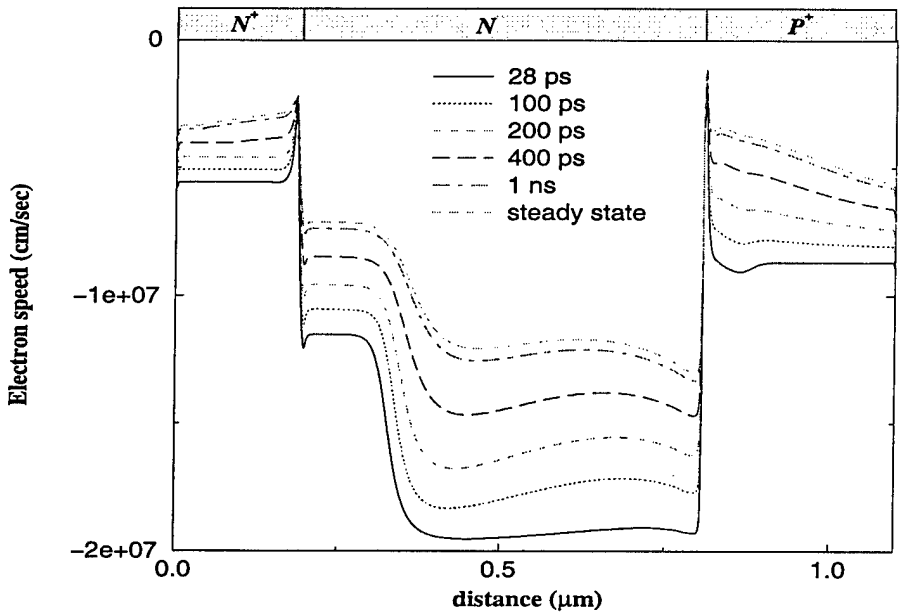

Figure 4.33: *Electron velocity evolution*

4.0.6 Simulation of a *4H-SiC* diode

We have performed a simulation of a *4H-SiC* diode, in order to check if there are significant differences between the two polytype. The electrical response of the two system has been found to be very similar (fig. 4.35). With respect to the 6H, the 4H-SiC displays a larger tunneling contribution due to the fact that the donor and acceptor levels are shallower ($E_D = 0.065eV$ *and* $E_a = 0.191eV$). The carrier mobility of the two material is also different:

$$\mu_{n0} = 360\,cm^2/Vsec \quad and\ \mu_{n0} = 800\,cm^2/Vsec$$

$$\mu_{p0} = 60\,cm^2/Vsec \quad e\ \mu_{p0} = 100\,cm^2/Vsec$$

. for 6H-SiC and 4H-SiC, respectively.

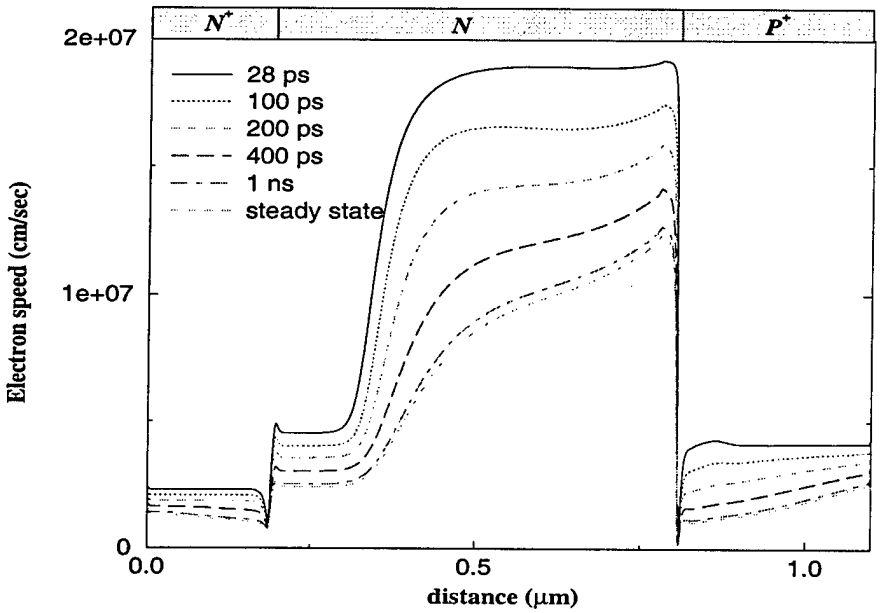

Figure 4.34: *Hole velocity evolution*

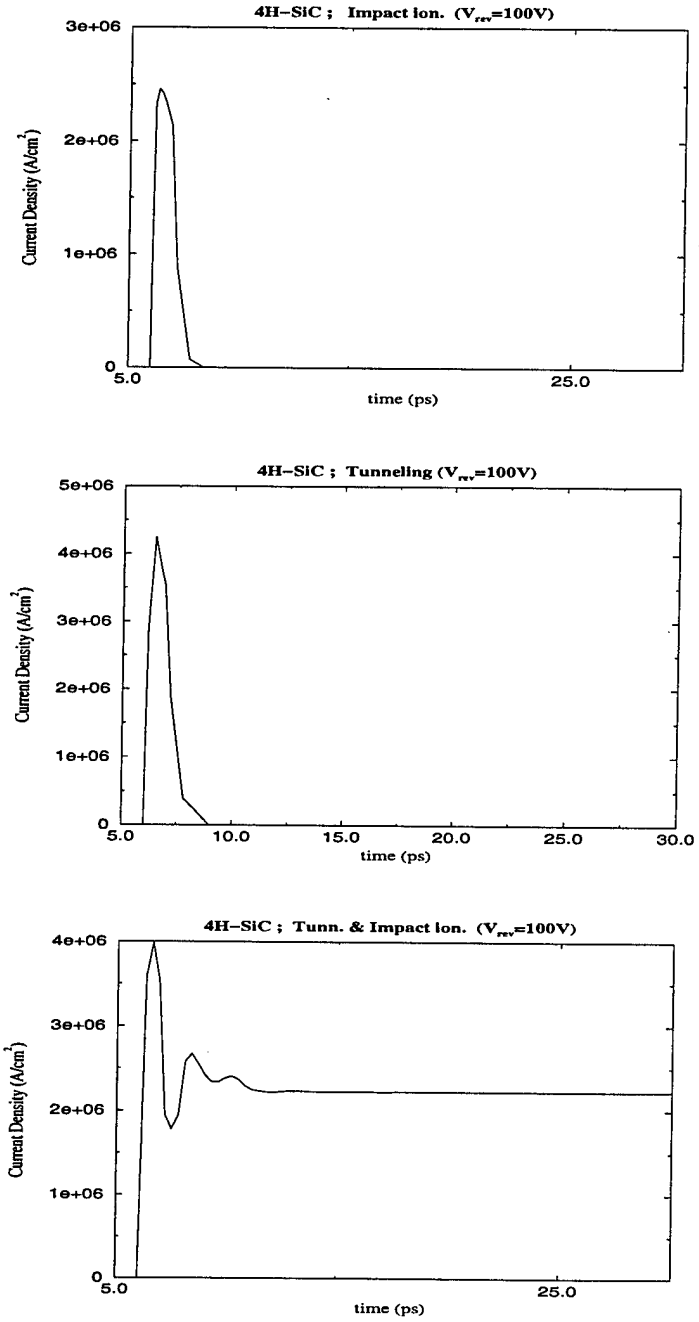

Figure 4.35: *Current density in 4H-SiC*

4.1 DC I-V characteristics

The stationary current-voltage characteristics for 6H-SiC extracted from the time dependent simulations are presented in fig.4.36).

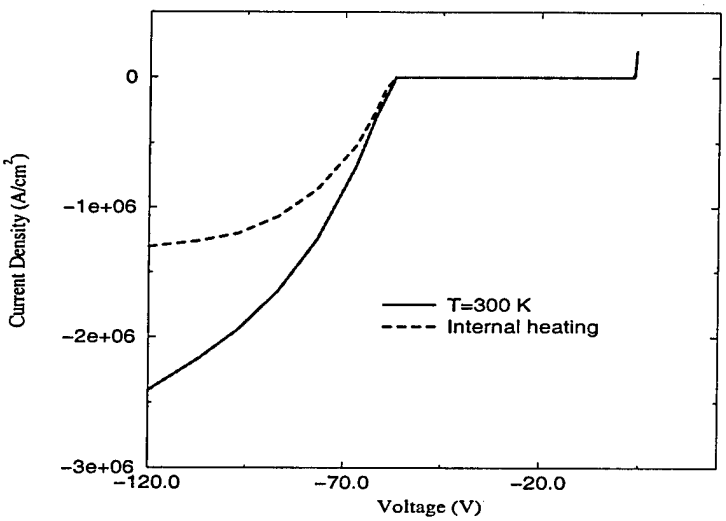

Figure 4.36: *I-V Characetristics*

The two curves refer to a simulation at constant temperature (solid line) and one where internal heating is accounted for (dashed line). While the onset of the breakdown is similar in the two cases, when the internal temperature is considered we observe a slower current rise.

The actual value of the breakdown voltage is lower than the experimental one due to the smaller dimension of the diode considered in the simulation.

From fig. 4.37 we can infer that at higher temperatures the breakdown voltage tens to incraese. Thus, the conlcusion of our study is that the negative temperature inization coeffiecient resulting from the experimental analysis of 6H-SiC diodes cannot be attributed to internal physical mechanisms, but probably to technological problems.

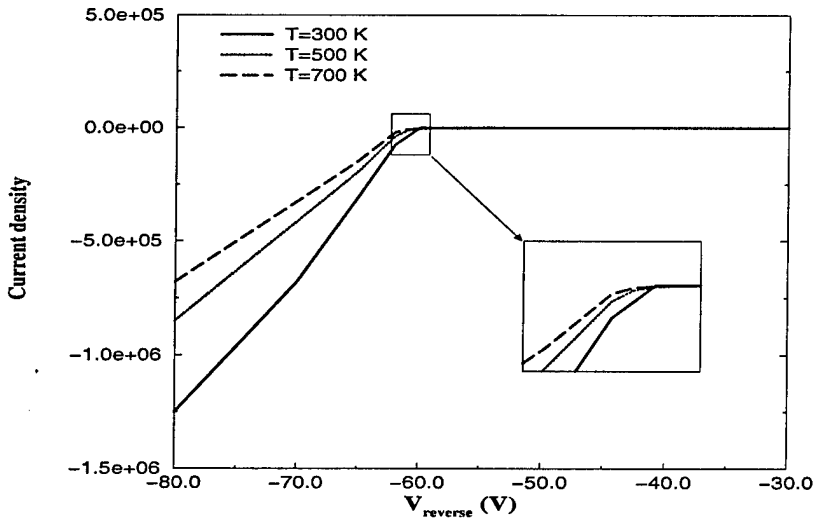

Figure 4.37: *IV characteristics of a 6H-SiC diode at different temperatures*

Bibliography

[1] P.Neudeck, C.Fazi *IEEE Elect. Devices Lett.* vol.18, n.3, March 1997, pag.96.

[2] M.Lundstrom *Modular series on solid state devices* vol.10, pag.171.

[3] S.M.Sze *Physics of Semiconductor Devices.*

[4] L.D.Landau, Lifshitz, *Kvantovaya Mechanika* Moskva 1974.

[5] *Silvaco International User's Manual.*

[6] S.Selberherr, *Analysis and Simulation of Semiconductor Devices* Wien: Springer-Verlag, 1984, pag.42.

[7] M.Bakowski et al. *Simulation of SiC High Power Devices* Phys. stat. sol. (a) vol.162,p.421 (1997)